J. Fluid Mech. (2007), *vol.* 572, *pp.* 433–469.
doi:10.1017/S0022112006003521 Printed in the United Kingdom

Instability of a chemically dense layer heated from below and overlain by a deep less viscous fluid

By CLAUDE JAUPART[1], PETER MOLNAR[2] AND ELIZABETH COTTRELL[3]

[1]Institut de Physique du Globe de Paris, Paris, 75252 Cedex 05, France

[2]Department of Geological Sciences, Cooperative Institute for Research in Environmental Science (CIRES), University of Colorado at Boulder, Boulder, CO 80309-0399, USA

[3]Lamont-Doherty Earth Observatory of Columbia University, Palisades, NY 10964, USA

(Received 15 July 2005 and in revised form 2 August 2006)

Near the threshold of stability, an intrinsically denser fluid heated from below and underlying an isothermal fluid can undergo oscillatory instability, whereby perturbations to the interface between the fluids rise and fall periodically, or it can be mechanically stable and in thermal equilibrium with heat flux extracted by small-scale convection at the interface. Both the analysis of marginal stability and laboratory experiments in large-Prandtl-number fluids show that the critical Rayleigh number, scaled to parameters of the lower fluid, depends strongly on the buoyancy number, B, the ratio of the intrinsic density difference between the fluids and the maximum density difference due to thermal expansion. For small buoyancy number, $B < \sim 0.1$, the critical Rayleigh number, Ra_C, for oscillatory instability is small $Ra_C < \sim 50$, and increases steeply for $B \sim 0.25$. For $B > \sim 0.5$ and $Ra_C > \sim 1100$, a second form of instability develops, in which convection is confined to the lower layer. The analysis of marginal stability for layers with very different viscosities shows further that two modes of oscillatory instability exist, depending on the value of B. For $B < 0.275$, the entire lower layer is unstable, and wavelengths of perturbations that grow fastest are much larger than its thickness. For $B > 0.275$, only the bottom of the lower layer is buoyant, and instability occurs by its penetrating the upper part of the lower layer; the wavelengths of the perturbations that grow fastest are much smaller than those for $B < 0.275$, and the maximum frequency of oscillatory instability is much larger than that for $B < 0.275$. Oscillations in the laboratory experiments show that the heights to which plumes of the lower fluid rise into the upper one increase with the Rayleigh number. Moreover, in the finite-amplitude regime, the oscillation is not symmetrical. Plumes that reach maximum heights fall quickly, folding on themselves and entraining some of the upper fluid. Hence oscillatory convection provides a mechanism for mixing the fluids. Applied to the Earth, these results bear on the development of continental lithosphere, whose mantle part is chemically different from the underlying asthenosphere. As shown by the laboratory experiments and stability analysis, the lithosphere can be mechanically stable and in thermal equilibrium such that heat supplied by small-scale convection at the top of the asthenosphere is conducted through it. The lithosphere seems to have developed in a state near that of instability with different thicknesses depending on its intrinsic buoyancy. It may have grown not only by chemical differentiation during melting, but also by oscillatory convection entraining chemically denser material from the asthenosphere.

1. Introduction

Despite the nearly homogeneous chemical composition of the Earth's mantle, chemically distinct layers mark its top and apparently also its bottom. A chemically distinct bottom of the Earth's mantle not only may account for the large lateral heterogeneity in seismic wave speeds there (Lay *et al.* 1997), but also may play a key role in the formation of mantle plumes, which manifest themselves as localized sources of volcanism at the Earth's surface (e.g. Davaille, Girard & Le Bars 2002; Jellinek & Manga 2002, 2004; Le Bars & Davaille 2004). Chemical differences between boundary layers at the top of the upper mantle beneath continents and oceans seem to have played a crucial role in the preservation of continental regions throughout nearly the entire 4.45 Ga age of the Earth, compared with rapid replacement of oceanic plates on times scales of 200 Myr. With these aspects of Earth history in mind, we undertook a study of the role that chemical differences play in what is largely thermally induced convection in the mantle.

The strong temperature dependence of viscosity in the Earth makes its top boundary layer, the lithosphere, sufficiently strong that it behaves rigidly on geologic time scales. This simple property of rock-forming minerals enables lithospheric plates to span horizontal distances that, unlike the case for Rayleigh–Bénard convection, do not scale with the depth of the convecting region. The strength of the plates, therefore, plays a crucial role in enabling them to remain at the Earth's surface for long durations, instead of being swept into downwelling plumes or sheets. The oldest parts of lithospheric plates, within ancient continents, seem, however, to have relied also on chemical differences for their preservation (e.g. Jordan, 1975, 1978, 1988).

Melting and separation of the melt from the mantle to form continental crust leaves a residue with a somewhat lower density than the mantle beneath it. Thus, ancient lithosphere with its relatively low density forms the thickest lithospheric plates on Earth and studies of diamonds and other minerals erupted through it show that thick lithosphere formed early in Earth's history, more than 3×10^9 years ago (e.g. Richardson *et al.* 1984; Pearson *et al.* 1995; Carlson *et al.* 2000). Younger continental lithosphere is thinner and also intrinsically denser (e.g. Poudjom Djomani *et al.* 2001). We contend that the difference in thickness, composition and density between ancient and younger lithosphere reflects the effects of chemically induced, intrinsic density differences on convective stability (Cottrell, Jaupart & Molnar 2004).

To understand how this low-density lithosphere formed, and the role that chemical differences play in sustaining it, requires an understanding of how convection, including convective instability, occurs in a fluid whose density depends, not only on temperature, but also on composition. The role of chemical differences in fluids has received much attention in analyses of doubly diffusive convection, in which both temperature and chemical differences diffuse through a fluid, for instance in studies of salt fingers in the ocean (e.g. Worster 2004) and of magmas (Jaupart & Tait 1995). The role of chemical differences in mantle-wide convection has recently generated interest because of the wealth of dynamic regimes allowed (Davaille 1999*a*, *b*; Jellinek & Manga 2002, 2004; LeBars & Davaille 2002; Zaranek & Parmentier 2004). The difficulty in determining the magnitude of intrinsic density contrasts in the Earth mantle, however, has limited the applicability of these studies. It is perhaps surprising that the one part of the Earth mantle where intrinsic density differences can be determined through direct sampling, the lithosphere, has received so little attention. These limits motivated the present study of convection in a layered medium with two chemically different fluids and therefore with different intrinsic densities, which is cooled from above or heated from below. Cottrell *et al.* (2004) presented preliminary

results. Here we discuss marginal stability and describe laboratory experiments, which are of general interest because they both illustrate well a form of oscillatory convection.

Although oscillatory instability has been known as a general concept for more than 100 years (e.g. Drazin & Reid 1981, p. 12), Richter & Johnson (1974) showed in a study applied to the Earth how the addition of an intrinsic density difference, due to chemical differences between layers, can lead to oscillatory convective instability. Such oscillatory instability has also been observed in the laboratory experiments of Davaille (1999*a*) and Le Bars & Davaille (2002, 2004).

1.1. *The Earth's lithosphere*

Oceanic lithosphere thickness varies as a function of age and reaches a maximum of about 100 km, but continental lithosphere can be as thick as 250 km beneath Archean cratons (Rudnick, McDonough & O'Connell 1998; Jaupart & Mareschal 1999; Gung, Panning & Romanowicz 2003). The density of the continental lithosphere determined directly using xenoliths at atmospheric pressure and temperature appears to vary with age, from $3.31\,\mathrm{Mg\,m^{-3}}$ for Archean material (4.0 to 2.5 Ga) to $3.36\,\mathrm{Mg\,m^{-3}}$ for the Phanerozoic era (since $\sim$600 Ma). In comparison, the density of the underlying convecting mantle at the same temperature and pressure is estimated to be $3.39\,\mathrm{Mg\,m^{-3}}$ (Poudjom Djomani *et al.* 2001). These results indicate that the continental lithosphere down to its base is intrinsically buoyant (i.e. because of its chemical composition) with respect to the convecting mantle, a result corroborated by studies of large-scale gravity and geoid anomalies (e.g. Doin, Fleitout & McKenzie 1996). The intrinsic buoyancy, defined as $\Delta\rho_c/\rho_0$, where $\Delta\rho_c$ is the chemical density difference and ρ_0 a reference density for the mantle, takes values between about 1 % and 2.5 %. The intrinsic buoyancy thus varies from case to case, but so does lithosphere thickness, from values as large as 250 km for Archean continents to about 150 km beneath continents younger than $\sim$600 Ma. Continental lithosphere of various ages, compositions and thicknesses appears to be stable, in contrast to that beneath oceans, which suggests the existence of multiple stable states (Cottrell *et al.* 2004).

The intrinsic buoyancy of continental lithosphere is not sufficient to guarantee its stability at the top of Earth's convecting mantle: lithosphere is cooled from above and hence develops a negative buoyancy. The temperature difference across the mantle lithosphere of about 1000 K induces a negative buoyancy contrast $\Delta\rho_T/\rho_0 \approx 4\,\%$, for a coefficient of thermal expansion of $4\times10^{-5}\,\mathrm{K^{-1}}$. The relevant parameter to characterize the density structure of the lithosphere is the buoyancy number $B = \Delta\rho_c/\Delta\rho_T$, with typical values of about 0.6 and 0.25 for Archean and Phanerozoic lithosphere, respectively. Because partial melting has dehydrated the continental lithosphere, it should be more viscous than the underlying convecting mantle (Kohlstedt, Evans & Mackwell 1995). The viscosity contrast may be as large as two orders of magnitude (Hirth & Kohlstedt 1996).

The stability of continents also involves heat transport mechanisms. In order to sustain the temperature difference of 1000 K across the mantle lithosphere, heat must be supplied from below. The most likely mechanism is small-scale convection in a thin basal boundary layer (Parsons & McKenzie 1978; Jaupart *et al.* 1998). Beneath the oceans, heat flux decreases away from mid-ocean ridges, owing to the conductive cooling of hot mantle that has risen toward the Earth's surface, and then settles to an almost constant value where oceanic crust is older than $\sim$100 Ma (Parsons & Sclater 1977; Lister *et al.* 1990). This dependence of heat flux on age reflects an initial phase of conductive cooling followed by convective breakdown of a thin thermal

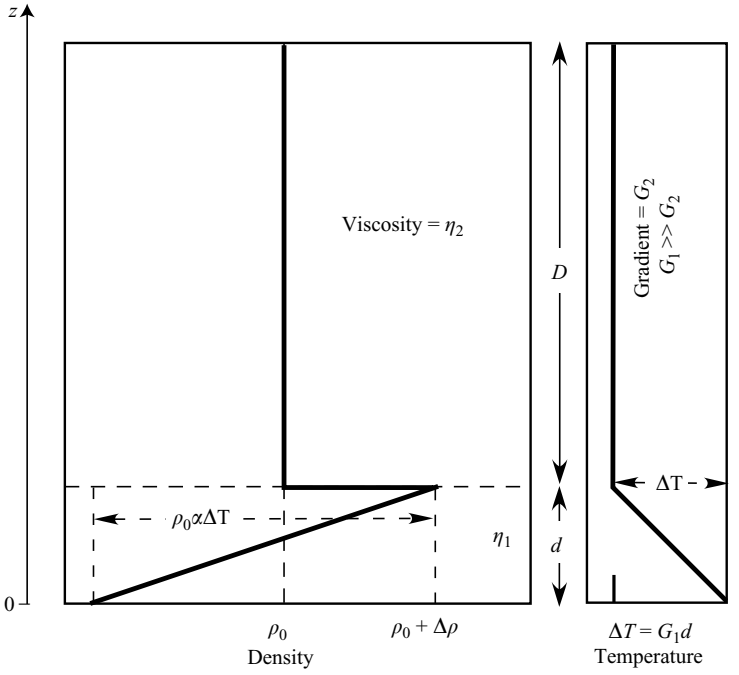

FIGURE 1. Initial temperature and density structures assumed in calculations of marginal stability. Heat is conducted into the base of a fluid that is intrinsically denser by an amount $\Delta\rho$. The temperature at the base is warmer by ΔT_1 than the fluid above it, across which a very small temperature gradient G_2 is assumed. We assume a linear gradient through the lower layer, $G_1 = \Delta T_1/d$. We also allow for different viscosities of the two layers.

boundary layer at the base of a layer stabilized by its low temperatures and its large viscosity (e.g. Parsons & McKenzie 1978). Heat supplied by intermittent breakdown of this thin boundary layer accounts for the steady-state thermal structure of old oceanic lithosphere. This process has been reproduced in the laboratory in fluids with strongly temperature-dependent viscosity (Davaille & Jaupart 1993, 1994). In these experiments, the contrasting heat transport mechanisms, from conduction at the top to small-scale convection at the base of the thermal boundary layer, are due only to the large viscosity difference between top and bottom. In the case of continents, an intrinsic buoyancy contrast may also contribute to contrasting heat transport mechanisms, but to our knowledge, the feasibility of this mechanism has not been ascertained in the laboratory.

1.2. *Basic assumptions*

We seek an understanding of how chemical differences between lithosphere and asthenosphere affect the convective stability of the lithosphere and its evolution. Thus, we seek an understanding of how an intrinsic density difference between two layers affects convective instability of one of the layers, when the other is stable. Because of the difficulties in setting initial conditions in the laboratory, we consider a configuration opposite to that in the Earth: we impose a temperature gradient across a chemically heavier, but more viscous bottom layer that underlies an intrinsically lighter, nearly isothermal layer (figure 1). If sufficiently warm, the density of the lower layer can be less than that of the upper layer, and hence the lower layer can become unstable.

For analysis of marginal stability, we simply assumed that the initial, uniform temperature gradient across the two layers was very different (figure 1):

$$T_j(z) = -G_j(z - d), \tag{1}$$

where $j = 1, 2$, with the subscript 1 referring to the lower layer $z \leqslant d$ and 2 to the upper layer $z \geqslant d$, and $G_1 \gg G_2$; d is the thickness of the basal high-density layer. Thus, the temperature drop across the lower layer is $\Delta T_1 = G_1 d$. This temperature structure includes a discontinuity in heat flux at the interface between the layers, and in reality, a thermal boundary layer would develop there. As discussed below, we contend that this boundary layer has only a minor effect on the thermal structure and resulting flow, and we will use laboratory experiments to verify this.

Other difficulties render the simple structure shown in figure 1 as only approximate for the laboratory experiments. Thermal steady state requires that heat be extracted from the lower layer with a heat flux that is equal to the basal heat supply, and the same amount of heat must be removed from the upper layer. In the laboratory, we used a thick upper layer that was thermally insulated at the top; hence the layer warmed gradually. As we show below, the heating rate was so small that it allowed quasi-steady-state thermal conditions in the lower layer; the change of mean temperature in the upper layer occurred over a time scale that was large compared to the diffusive time scale of the lower layer. A similar set of conditions apply in the Earth, where heat loss through the Earth's surface only partially balances radiogenic heat production in the crust and mantle, and this slow heat loss induces slow secular cooling of the Earth's interior.

Consider a thin fluid layer of thickness d with viscosity η_1 below a large volume of fluid with viscosity η_2. In steady state, the heat flux conducted through this thin basal layer across which the temperature drop is ΔT_1, must equal the flux transported by small-scale convection in the upper liquid, Q_2:

$$Q_2 = k\frac{\Delta T_1}{d}, \tag{2}$$

where k is the coefficient of thermal conductivity, assumed to be the same in the two layers. Following Howard (1966), we may assume that, in the thick upper fluid, convection proceeds by intermittent breakdown of a thin thermal boundary layer. Thus, the heat flux across the boundary layer is given by:

$$Q_2 = Ck\left(\frac{\alpha\rho g}{\kappa\eta_2}\right)^{1/3}\Delta T_2^{4/3}, \tag{3}$$

where C is a constant that takes a value of 0.21 ± 0.02 (Townsend 1964; Deardorff, Willis & Lilly 1969). Here, α is the coefficient of thermal expansion, g is gravity, ΔT_2 is the temperature drop across the thin boundary layer, κ is thermal diffusivity, and η_2 is the viscosity of the upper layer.

Defining $\Delta T = \Delta T_1 + \Delta T_2$ and $\varepsilon_i = \Delta T_i/\Delta T$ and setting Q_2 in (2) and (3) equal yields:

$$\frac{1-\varepsilon_2}{\varepsilon_2^{4/3}} = C\left(\frac{\alpha g\rho\Delta T d^3}{\kappa\eta_1}\right)^{1/3}\left(\frac{\eta_1}{\eta_2}\right)^{1/3} = CRa^{1/3}\left(\frac{\eta_1}{\eta_2}\right)^{1/3}, \tag{4}$$

where Ra is a Rayleigh number. If $\eta_1/\eta_2 \gg 1$, then $\varepsilon_2 \ll 1$, and the temperature difference across the boundary layer is a small fraction of the total. Typical conditions for the continental lithosphere and our laboratory experiments are such that $\eta_1/\eta_2 \approx 10^2$ and $10^2 < Ra < 10^3$, implying that $0.16 \leqslant \varepsilon_2 \leqslant 0.27$. For simplicity,

we shall neglect the thin unstable thermal boundary layer in our analysis and will assess the validity of this assumption by a comparison between marginal stability calculations and laboratory experiments.

2. Calculation of marginal stability

2.1. *Procedure*

As noted above, in the analysis of marginal stability, we ignore the thermal boundary layer at the interface between the layers. The temperature drop across the lower layer is $\Delta T_1 = G_1 d$. With the interface between the layers at $z = d$, the density within each layer is given by:

$$\rho_1(z) = \rho_0[1 + \alpha G_1(z - d)] + \Delta\rho \quad (z \leqslant d), \tag{5a}$$

$$\rho_2(z) = \rho_0[1 + \alpha G_2(z - d)] \quad (d \leqslant z \leqslant d + D), \tag{5b}$$

where D is the thickness of the less dense, nearly isothermal layer.

As we are interested in cases where the gradient across the upper layer is negligible, we consider only cases in which $|G_1| \gg |G_2|$.

As is traditionally done (e.g. Chandrasekhar 1961; Le Bars & Davaille 2002) and described more fully in Appendix A, we linearized the momentum and heat transfer equations about a state of no motion and we assumed an incompressible fluid in the equation of continuity. We find solutions, in the form of a sum of eigenfunctions, to the linear differential equation governing flow within each layer, subject to harmonic perturbations, and we assume that these perturbations grow exponentially with time, e^{st}, with a growth rate factor s. To determine the critical Rayleigh number at the threshold of instability, we followed standard procedure (Appendix A).

Six dimensionless numbers govern the solution for instability of flow with the two-layered structure that we consider: the Rayleigh number defined in terms of the parameters in layer 1

$$Ra_1 = \frac{\alpha g \rho G_1 d^4}{\kappa \eta_1}, \tag{6}$$

the Prandtl number, which we treat as infinitely large and hence ignore; the buoyancy number, B, which scales the intrinsic density difference, $\Delta\rho$, to that due to thermal expansion, $\rho_0 \alpha \Delta T_1 = \rho_0 \alpha G_1 d$:

$$B = \frac{\Delta\rho}{\rho_0 \alpha \Delta T_1}, \tag{7}$$

and three ratios: of the thicknesses of the layers, D/d; of the viscosities of the layers $\gamma = \eta_1/\eta_2$; and the temperature gradients across the layers, G_2/G_1. We are not interested in the role of different temperature gradients in the upper layer, and in Appendix B we show that for sufficiently small ratios G_2/G_1, results become independent of G_2. Thus, only four dimensionless numbers are important: Ra_1, B, γ and D/d.

The inclusion of an intrinsic difference in density between the layers allows the growth rate to be complex: $s = \sigma + i\omega$. At marginal stability, the real part of the growth rate must vanish ($\sigma = 0$), but the imaginary part, ω, which defines the angular frequency of an oscillating flow, need not vanish. In addition to the critical Rayleigh number, Ra_C, and the wavenumber of the perturbation, k_C, for which Ra_1 is a minimum, we also find a corresponding angular frequency ω_C. Thus, we seek the

family of values of Ra_C, k_C and ω_C as functions of the buoyancy number B, the ratio of viscosities γ, and the ratio of layer thicknesses D/d.

Our analysis complements several previous studies of convection with two chemically different layers at Rayleigh numbers that were much larger than Ra_C (e.g. Olson & Kincaid 1991; Tackley 1998; Gonnermann, Manga & Jellinek 2002; Jellinek & Manga 2002, 2004; Namiki 2003; Namiki & Kurita 2003; Zhong & Hager 2003; McNamara & Zhong 2004*a*, *b*, 2005; Wenzel, Manga & Jellinek 2004). Most of these studies focused on the entrainment of a dense basal layer for values of $B > 0.5$. A few other studies have dealt with oscillatory instability in other configurations. Zaranek & Parmentier (2004) considered a linearly varying intrinsic density across a layer initially with a linear temperature profile. Hsui & Riahi (2001) considered linear stability where chemical differences can induce oscillatory instability. Houseman & Houseman (2006) analysed the instability of thickened crust overlying a mantle lithosphere whose density depends on its thermal structure.

2.2. *Test: Comparison with results of Currie* (1967)

To test our solutions, we compare results with those of Currie (1967), who analysed the stability of a homogeneous layer of fluid heated at its base over a finite time, and hence affecting only the lowermost part of the layer. He used the same temperature profile as that of figure 1 and hence we solve the same problem if we set $B = 0$. Currie (1967) intended to determine the onset of instability in a fluid that is suddenly heated at its base by the imposition of a constant temperature there. In such thermal conditions, the vertical temperature profile before instability has marked curvature and it is not clear that the approximation of a linear gradient over a thin sub-layer is appropriate. As discussed above and as we shall see in the laboratory experiments, we are dealing with a lower layer that is denser than the overlying fluid, which allows thermal steady state in certain conditions. Here, we are not interested in the validity of Currie's approximation for the heating of a homogeneous fluid layer and merely use his results to check the accuracy of our calculations in the limit of $B = 0$.

Currie (1967) reported that in the limit of $d \ll D$, the critical Rayleigh number dropped to 32 (this value was obtained numerically to two significant digits), much smaller than the values associated with Rayleigh–Bénard convection. We obtained the same result (figure 2). In fact, for $\gamma > 1$, Ra_C decreases further to values as small as 28. Qualitatively this can be understood as analogous to Rayleigh–Bénard convection, in which the critical Rayleigh number is smallest for free-slip boundaries, intermediate for mixed boundaries, and largest for no-slip boundaries (e.g. Pellew & Southwell 1940); as γ increases, the interface becomes effectively stress free. Neither Ra_C nor $k'_C = k_C d$ depend strongly on γ, provided it is at least 10. However, figure 2 reveals, as Currie (1967) also found, that for $\gamma = 1$, as the ratio of thicknesses D/d increases, the value of k'_C decreases and approaches zero. The wavenumber for maximum growth rate, therefore, depends on the thickness of the upper, nearly isothermal layer. We solved the problem with a finite gradient in the upper layer instead of with a zero gradient in an infinite upper layer because we could not find a solution for $\gamma = 1$ and an infinite upper layer, presumably because it requires that $k'_C \to 0$.

2.3. *Influence of the buoyancy number on the conditions for marginal stability*

Our analysis follows that of Le Bars & Davaille (2002, 2004), who considered a pair of layers with two intrinsically different densities and initially with a uniform temperature profile across the pair of layers, like that for marginal stability of Rayleigh–Bénard convection. We observed phenomena qualitatively similar to what they and Richter & Johnson (1974) noted (figure 3). First, three regions near the threshold of instability

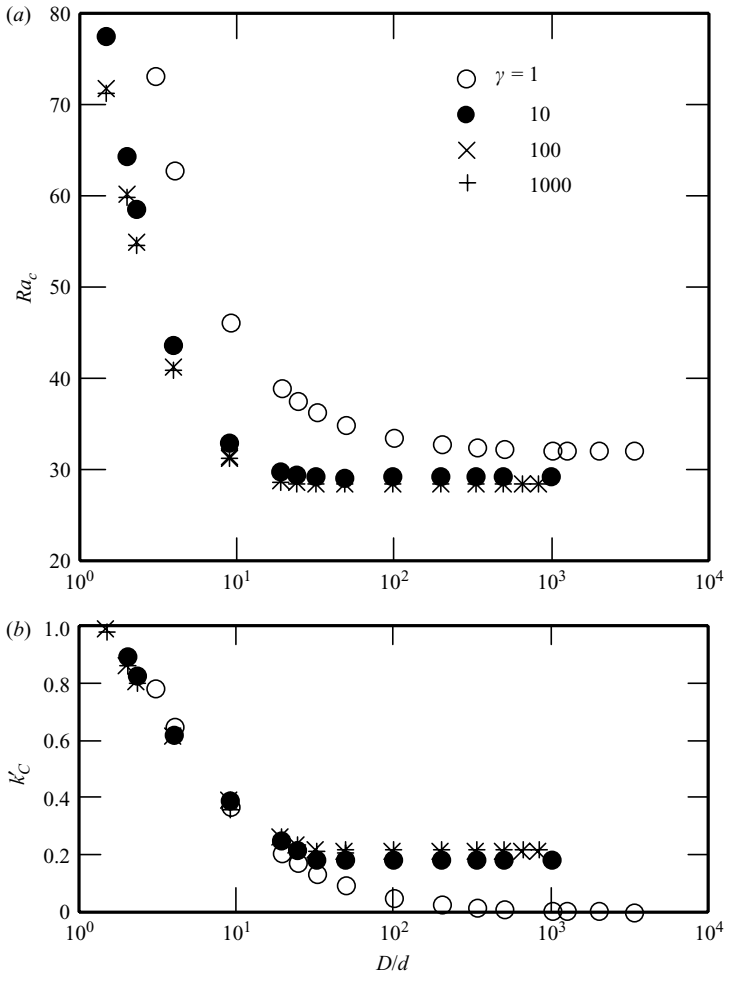

FIGURE 2. Dependences of (*a*) the critical Rayleigh number Ra_C and (*b*) the corresponding dimensionless wavenumber k'_C on the ratio of the thicknesses of the layers D/d, for $B = 0$ and for different ratios of viscosities, γ. Note that for $\gamma = 1$, and sufficiently large values of D/d, $Ra_C \rightarrow 32$, as Currie (1967) reported, but $k'_C \rightarrow 0$. For $\gamma \geqslant 10$, $Ra_C \rightarrow 28$, and k'_C remains finite.

exist. By definition, for low Rayleigh number ($Ra_1 < Ra_c$), both layers are stable. For low B ($< \sim 0.5$) and $Ra_1 > Ra_c$, an oscillatory instability develops, such that laterally harmonic perturbations to the interface between the layers rise and fall periodically in time. For large B ($> \sim 0.5$) and $Ra_1 > Ra_c$, convection can occur within the lower layer with negligible displacement of the interface between the layers. The critical Rayleigh number depends strongly on B for $B < \sim 0.5$; the (dimensionless) angular frequency $\omega'_C = \omega_C \eta_1 / \rho_0 \alpha \Delta T_1 g d$ varies from zero at $B = 0$ (there is no oscillatory instability without a finite intrinsic density difference) to a maximum and again approaches zero as B approaches ~ 0.5 (Le Bars & Davaille 2002; Cottrell *et al.* 2004). For an oscillatory instability ($B < \sim 0.5$), the dimensionless wavenumber, k'_C, of an infinitesimal perturbation is smaller than that for which convection is confined to the bottom layer ($B > \sim 0.5$).

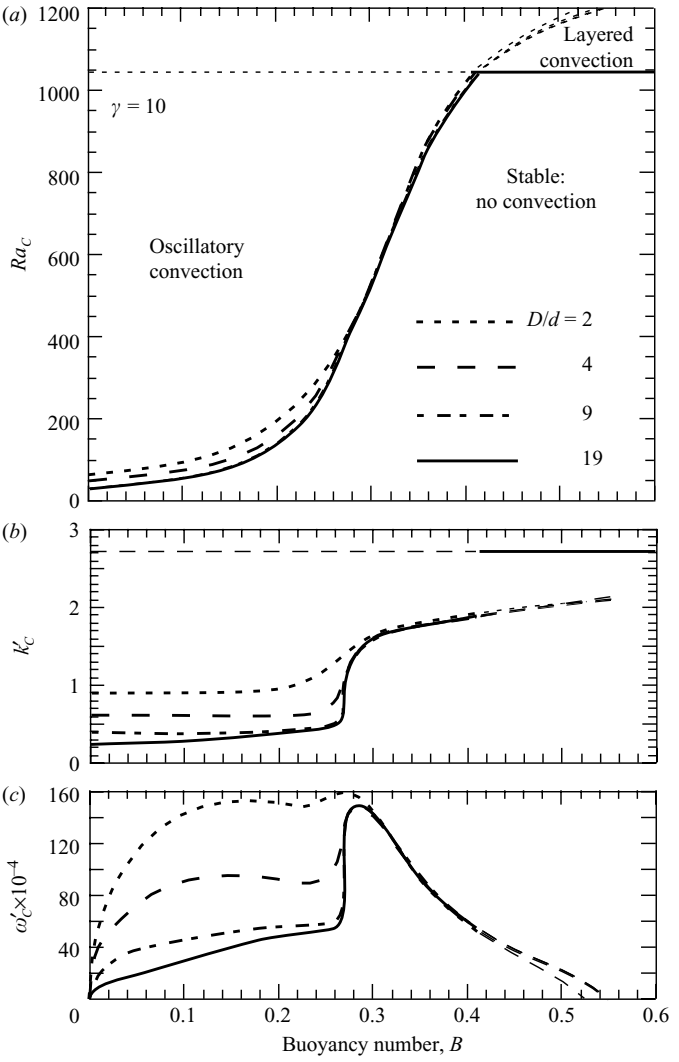

FIGURE 3. Dependences of (*a*) the critical Rayleigh number Ra_C, (*b*) the dimensionless wavenumber k'_C at which Ra_C is a minimum, and (*c*) the corresponding dimensionless angular frequency of the oscillatory instability ω'_C on the buoyancy number B, for $\gamma = 10$ and for different values D/d. Note that three regimes exist: a stable regime where $Ra < Ra_C$, oscillatory convective instability for $B < \sim 0.5$, and layered convection within the lower layer for $B > \sim 0.4$. (Layered convection is a form of Rayleigh–Bénard convection, but with a top boundary condition that is neither stress-free nor no-slip.)

We made calculations for layers with a variety of viscosity ratios, γ, and for different ratios of layer thicknesses. Several features of the various dependences of Ra_C, k'_C and ω'_C on B (figures 3 and 4) differ from what Le Bars & Davaille observed. For large γ ($\geqslant 10$), for $0 < B < \sim 0.27$, both k'_C and ω'_C are markedly smaller than they are for $\sim 0.3 < B < 0.5$. As the ratio of the layers, D/d increases, the dependence of all of Ra_C, k'_C and ω'_C on B differ little. Similarly, for $\gamma = 10$ or 100, the dependence of all of Ra_C, k'_C and ω'_C on B are virtually identical (figure 4). Perhaps, most important, the very different values of k'_C and ω'_C for values of $B > \sim 0.3$, and $B < \sim 0.25$, and the

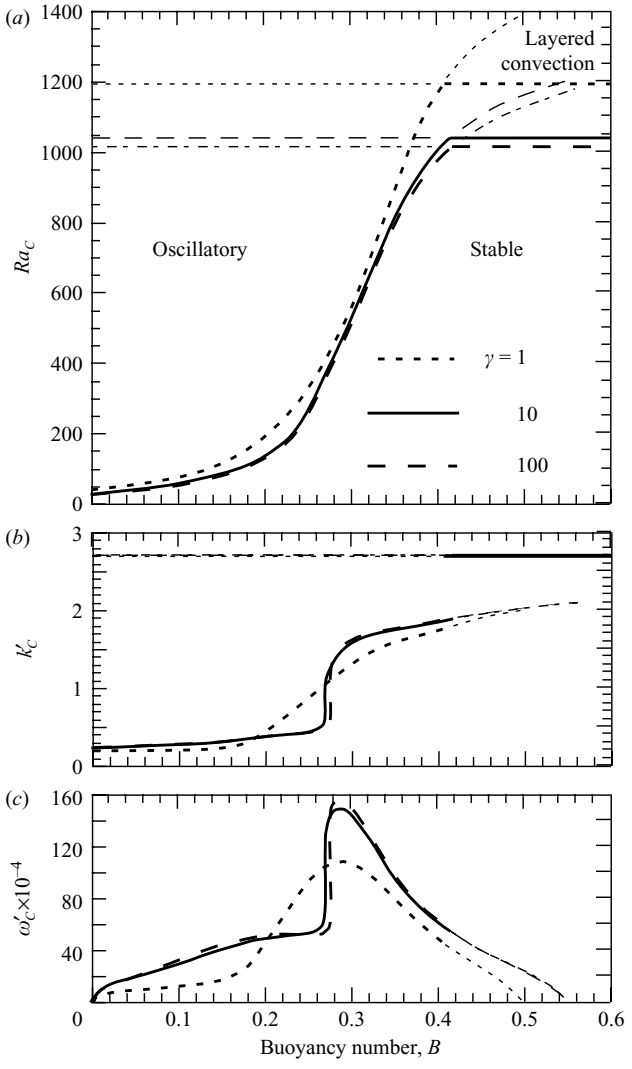

FIGURE 4. Dependences of (*a*) the critical Rayleigh number Ra_C, (*b*) the dimensionless wavenumber k'_C at which Ra_1 is a minimum, and (*c*) the corresponding dimensionless angular frequency of the oscillatory instability ω'_C on the buoyancy number B, for $D/d = 19$ and for different values γ. As in figure 3, three regimes exist, but notice that the critical Rayleigh number for the stable regime depends on γ. It is smaller as γ increases, because in effect the top boundary of the lower layer becomes increasingly like a free boundary as γ increases. For large γ, Ra_C approaches 1100.65, appropriate for Rayleigh–Bénard convection with one free and one no-slip boundary (Pellew & Southwell 1940). For large B, where layered convection would occur, extrapolations of curves to higher Rayleigh numbers are shown with finer dashed lines.

rapid increase in Ra_C for $0.25 < B < 0.30$ suggests that two different modes, or flow patterns, develop for the two ranges of the buoyancy number B.

2.4. *Different modes: analysis of eigenfunctions*

To ascertain whether different modes exist, we calculated appropriate linear combinations of eigenfunctions that describe the vertical component of velocity for different values of B, γ and D/d. Because of their arbitrary scaling, we normalized solutions

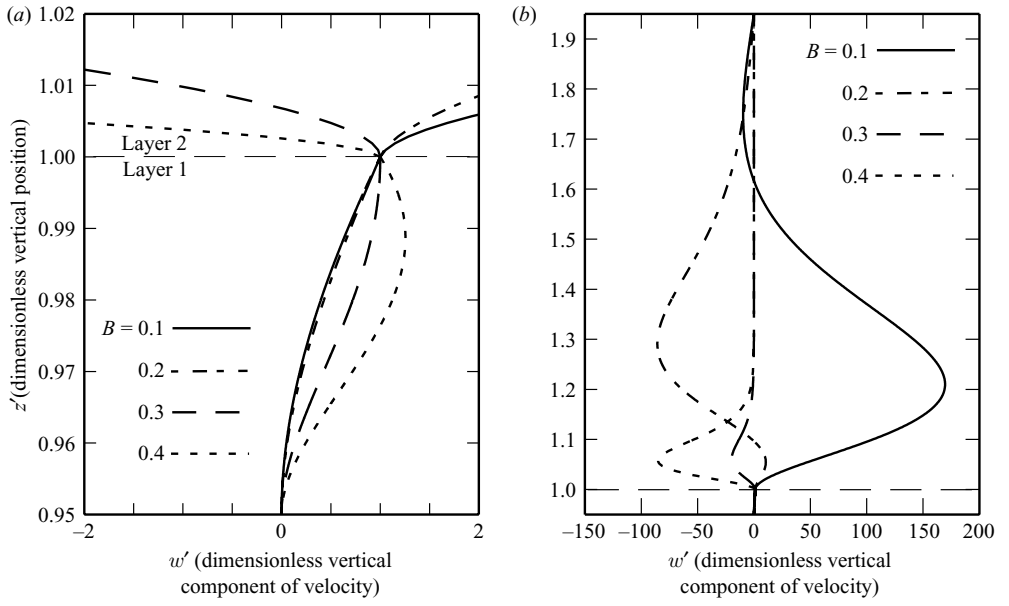

FIGURE 5. Calculations of w', the vertical component of velocity, at the threshold of instability for different values of B and for $\gamma = 100$ and $D/d = 19$. (*a*) w' is plotted for only the lower layer and a part of the upper layer. For $B < \sim 0.25$, the form in the lower layer is almost independent of B, but for $B > \sim 0.25$, w' depends strongly on B with the maximum value of w'occurring in the lower layer. (*b*) Values of w' are shown for both layers.

of the (dimensionless) vertical component of velocity so that all equal one at $z = d$, the interface between the two layers.

For all cases of an oscillatory convective instability, if fluid rises or subsides at the interface it does so throughout the lower layer (figure 5). For the small values of B ($< \sim 0.25$), eigenfunctions increase monotonically from the base of the lower layer to the interface, and the z-dependence of vertical speed is approximately linear with height in the layer. Thus, where the interface rises, the material in the layer below stretches vertically and must contract horizontally to conserve mass. Rising parts of the lower layer are fed by horizontal flow within and throughout the lower layer. (Divergent flow accommodates subsiding flow where the interface is initially perturbed downward.)

For larger values of B ($> \sim 0.3$), vertical speed reaches a maximum within the upper part of the lower layer, not at the interface (figure 5). Accordingly, although the interface rises, near the top of the lower layer, fluid is compressed vertically: $\partial w/\partial z < 0$. Conservation of mass requires that $\partial u/\partial x > 0$; hence horizontal flow in the upper part of the lower layer is divergent and weakens the upward flow, rather than feeding it. Because all eigenfunctions are scaled to the same vertical speed at the interface, the increasingly divergent flow there with increased B causes a proportional increase in downward flow in the upper layer near the interface in figure 5. For this range of values of B, the instability develops because the hot basal part of the lower layer intrudes into the cooler upper part of that layer, which is buoyantly stabilized by the chemical difference.

The upper layer, with its negligibly small temperature gradient, should be convectively stable, and therefore, flow within it must be forced by flow in the lower layer, if assisted by perturbations to the temperature structure near the interface. To test

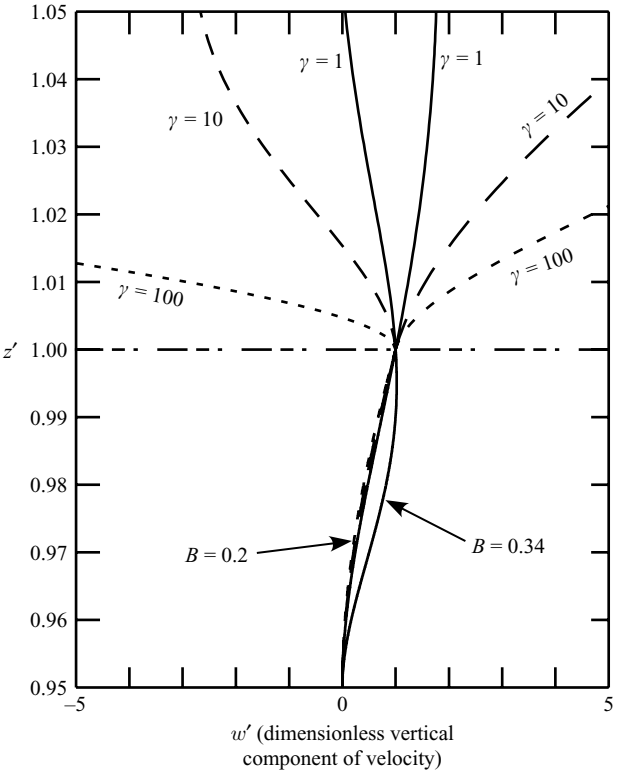

FIGURE 6. Calculations of w', the vertical component of velocity, at the threshold of instability for two values of B and for $\gamma = 1$, 10 and 100, for $D/d = 19$. Note that values within the lower layer ($z' < 1$) are virtually independent of γ, but in the upper layer they scale with γ. Flow in the upper layer is forced by that in the lower layer, and the lower the viscosity of the upper layer (larger γ), the faster the fluid moves there.

this, we calculated eigenfunctions for the same configuration but with $\gamma = 1$, $\gamma = 10$ and $\gamma = 100$. As shown for each of two values of B (figure 6), flow in the lower layer is virtually identical and independent of γ. By contrast, in the upper layer, the upward speed scales with γ, so that for smaller viscosity in the upper layer, flow is proportionally faster. Hence, flow within the lower layer is nearly insensitive to the properties of the upper layer, at least for $\gamma > 1$.

For small B, rising flow in the lower layer induces rising flow throughout much of the upper layer (figure 5); the positive buoyancy in both the lower layer and near the base of the upper layer, owing to the temperature perturbation, overwhelms the small chemically induced negative buoyancy. The flow throughout the upper layer must be different for different thicknesses of that layer. Thus, greater confinement of that flow by thinner upper layers will force maximum growth rates to occur at larger wavenumber and with higher frequency. For large B, however, slightly above the interface, flow reverses, and downward flow occurs above an upwardly perturbed interface (and correspondingly, upward flow overlies a downwardly perturbed interface). In all cases where flow reverses with height, a maximum vertical speed is reached either within the lower layer for the largest values of B, or just above the interface for intermediate values of B. As noted above, horizontal flow above the locus of maximum speed is divergent.

The analysis of eigenfunctions shows that for small B ($< \sim 0.25$), flow within the lower layer is simple, with monotonically increasing upward speed within the layer and rising flow above it. For large B ($> \sim 0.3$), however, the upward speed reaches a maximum within the lower layer, and the top part of that layer and the bottom of the upper layer stretch horizontally to accommodate flow from below.

3. Toward a simple physical understanding of the two modes of oscillatory flow

3.1. *Dependence of the pressure field and flow on buoyancy number B*

In the oscillatory mode, material from the hot chemically denser lower layer penetrates the colder, but chemically lighter upper layer, and to do so, its average density, $\Delta\rho_T = \rho\alpha\Delta T_1/2$, must be less than that of overlying material: $\Delta\rho_T > \Delta\rho_C$, or $B < \sim 1/2$, a result confirmed by calculations shown in figures 3 and 4.

To obtain a scaling relationship between Ra_C and B, we restrict discussion to two dimensions. The lower layer is perturbed by a harmonic deflection of the interface with small amplitude $\delta(x) = \delta \sin(kx)$, and temperature increases linearly across the lower layer between its base at $z = 0$ and its top at $z = d + \delta$ (figure 1):

$$\frac{\partial T}{\partial z} = \frac{\Delta T_1}{d + \delta} \quad (0 \leqslant z \leqslant d + \delta). \tag{8}$$

In the limit of large viscosity contrast, the upper fluid may be considered inviscid, such that it exerts no shear tractions on the lower layer and such that its pressure field is hydrostatic. For small deformation δ with wavelength larger than the layer thickness, the vertical component of velocity should be small and should contribute a negligible viscous stress in the vertical momentum balance. Thus, we consider the hydrostatic limit, in which pressure as a function of height z in a column is given by

$$P(x, z) = \rho_0 g(D - \delta) + (\rho_0 + \Delta\rho) g(\delta + d - z) - \tfrac{1}{2}\rho_0 \alpha \Delta T_1 g \left[\frac{z^2}{d + \delta} - 2z + d + \delta \right]. \tag{9}$$

Using the definition of B from (7) and taking the limit of small δ, we obtain:

$$\frac{\partial P}{\partial x} = \frac{\rho_0 \alpha \Delta T_1 g}{2} \left[\frac{z^2}{d^2} + 2B - 1 \right] \frac{\partial \delta}{\partial x}. \tag{10}$$

At $z = 0$:

$$\frac{\partial P}{\partial x} = \frac{\rho_0 \alpha \Delta T_1 g}{2} (2B - 1) \frac{\partial \delta}{\partial x}. \tag{11}$$

B must be smaller than $1/2$ for the hottest, bottom part of the layer to be unstable, as predicted by the very simple bulk buoyancy argument.

If $B < 1/2$, equation (10) shows that the horizontal pressure gradient changes sign at the level z_c:

$$z_c/d = \sqrt{1 - 2B}. \tag{12}$$

Near the top of the lower layer, where $z > z_c$, the signs of $\partial P/\partial x$ and $\partial \delta/\partial x$ are the same, showing that the pressure gradient opposes the deflection of the interface. This is easily understood by considering that fluid at the top of the chemically dense layer consists of relatively dense material at temperatures close to those in the overlying fluid. In this part of the denser layer, therefore, the dominant contribution to buoyancy is composition, such that the fluid is negatively buoyant, and this negative buoyancy exerts a pressure gradient that retards the horizontally convergent flow near the interface. In contrast, near the bottom of the chemically denser layer, for $z < z_c$,

lateral temperature differences dominate the contribution of chemical differences to the pressure gradient, and the signs of $\partial P/\partial x$ and $\partial\delta/\partial x$ are opposite. The pressure gradient due to deflection of the interface, therefore, drives flow that enhances the deflection. This flow sets up the oscillatory instability.

3.2. *Critical Rayleigh number as a function of buoyancy number for* $B \leqslant 11/40$

Beginning with momentum balance, we may solve for an approximation to the flow field. The horizontal component of this balance is expressed by:

$$0 = -\frac{\partial P}{\partial x} + \eta_1 \nabla^2 u \approx -\frac{\partial P}{\partial x} + \eta_1 \frac{\partial^2 u}{\partial z^2}. \tag{13}$$

Integrating (13) twice, using (11) and the boundary conditions that $u = 0$ at $z = 0$ and that at $z = d$, the shear stress vanishes, and therefore, $\partial u/\partial z = 0$, yields for the horizontal component of velocity:

$$u = \frac{\rho_0 \alpha g \Delta T_1}{4\eta_1} \frac{\partial \delta}{\partial x} z \left[\frac{z^3 - 4d^3}{6d^2} + (2B - 1)(z - 2d) \right]. \tag{14}$$

Oscillatory movement requires a restoring effect to act against the initial perturbation, which, for viscous flow with no inertia, must be diffusion of heat. Such diffusion smoothes horizontal temperature differences and hence decreases the driving pressure gradient. Thus, at the threshold of instability, the time scale for diffusion matches that for deformation of the interface. We use the equation of continuity to estimate w from (14). Evaluating it at $z = d$ (the interface), with the approximation that $\partial^2\delta/\partial x^2 = \delta/\lambda^2$, where λ is wavelength, yields

$$w = \frac{\rho \alpha g \Delta T_1}{120\eta_1} \frac{d^3}{\lambda^2} \delta (11 - 40B). \tag{15}$$

Finally, recognizing that $w = \partial\delta/\partial t$, a sensible time scale τ can be expressed as $\tau = \delta^{-1}\partial\delta/\partial t$. Equating τ to the diffusive time scale, λ^2/κ:

$$\frac{\rho \alpha g \Delta T_1}{120\eta_1} \frac{d^3}{\lambda^2} (11 - 40B) \sim \frac{\kappa}{\lambda^2}, \tag{16}$$

which implies, ignoring the factor of 120, that

$$Ra_C = \frac{\rho \alpha g \Delta T_1 d^3}{\eta_1 \kappa} \propto (11 - 40B)^{-1}. \tag{17}$$

This predicts that the critical Rayleigh number Ra_C increases with increasing B, as it does in the numerical calculations (figure 7). Moreover, this equation breaks down near $B = 11/40 = 0.275$, where the calculations (figures 3 and 4) suggest a change in regime.

3.3. *Critical Rayleigh number as a function of buoyancy number for* $B \geqslant 11/40$

For $B > 11/40$, the balance of flow is more complicated than for small B. As the analysis of eigenfunctions shows, counterflow occurs within the lower layer near the interface between the two different layers. Let us consider a perturbation to the initial temperature structure that varies across the lower layer similar to that in (8), but that also is greater in the lower part of the layer than in the upper part. This approach is motivated by the recognition that for $\sim 1/4 < B < \sim 1/2$, only the bottom of the chemically heavy layer is buoyant, and perturbations to its stratification might grow by penetration of this part of the layer into the overlying warmer, but chemically

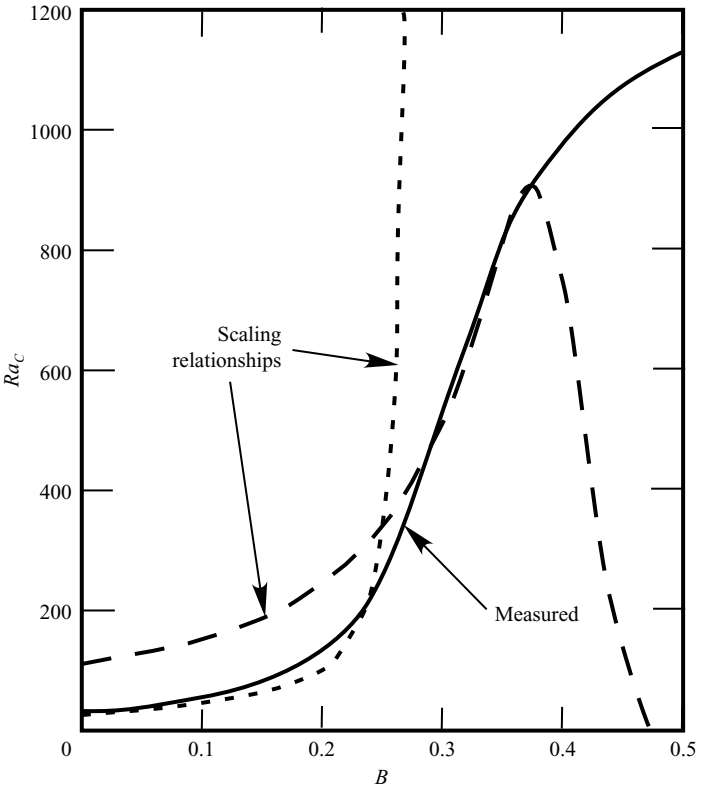

FIGURE 7. Comparison of scaling relationships derived in § 3.2 and 3.3 for Ra_C as a function of B. That for $B < \sim 0.25$ (short-dashed line) was obtained from (17) with a constant of proportionality set to 300. It exhibits the same upward curvature as do the calculated values and breaks down at $B = 11/40$ where the calculations indicate a change of regime (figure 4). That for $B > \sim 0.25$ (long dashed line) was obtained from (22) with a scaling factor of 33 and a value of 4 for parameter r. This second scaling relation matches the steep dependence of Ra_C on B for $0.3 < B < 0.38$, but fails to fit the larger range of B. $D/d = 19$; $\gamma = 100$.

similar part. To make the perturbation to the temperature structure of the lower layer greater near the bottom than the top of the layer, we consider a perturbation that includes non-uniform straining of the lower layer. To implement this, we let δ in (8) depend on height above the bottom, z:

$$\delta(z) = \delta \left[a + b\frac{z}{d} \right]. \tag{18}$$

Physically, we can interpret (18) as suggesting that the temperature field is strained so that the lower part of the bottom layer is stretched more than the upper part, as can be seen in the calculations of eigenfunctions (figure 5). Following the approach that led to (15), we now obtain:

$$w = \frac{\rho_0 \alpha g \Delta T_1}{\eta_1} \frac{d^3}{\lambda^2} \delta \left[a \left(\frac{11}{40} - B \right) + b \left(\frac{13}{120} - B \right) \right]. \tag{19}$$

To compare all conditions, we should assume that at $z = d$, δ in (15) is the same as it is in (19), and hence that $a + b = 1$. As a second condition to fix a and b, we assume that at below some fraction, r, of the level where pressure reverses sign,

$z_c = d\sqrt{1-2B}$, the temperature profile would be perturbed positively and above that height, it would be perturbed negatively:

$$a + rb\sqrt{1-2B} = 0. \tag{20}$$

Near the bottom where $z < rd\sqrt{1-2B}$, the perturbation to the temperature structure is large and makes these levels especially buoyant, but near the top of the lower layer where $z > rd\sqrt{1-2B}$, the temperature structure is compressed, and these levels are made less buoyant than for uniform stretching across the layer as in (8). Thus,

$$a = \frac{r\sqrt{1-2B}}{r\sqrt{1-2B}-1}, \quad b = \frac{-1}{r\sqrt{1-2B}-1}. \tag{21}$$

By analogy with the analysis that led to (17), for $B > \sim 1/4$, (19) leads to

$$Ra_C \propto \frac{r\sqrt{1-2B}-1}{r\sqrt{1-2B}\left(\frac{11}{40}-B\right)-\left(\frac{13}{120}-B\right)}. \tag{22}$$

As shown in figure 7, equation (22) can be made to fit part of the curve for Ra_C as a function of B, but not that for the largest values of B. The simple assumption for the perturbation in (18) is inadequate. At the same time, the analysis of eigenfunctions above (figure 5) suggests that flow occurs by selecting a velocity field for which the highest speed is not at the top of the basal layer, but within it, so that flow responds to a perturbation of temperature that is not uniform across the layer. The range of values of B over which (22) provides an adequate match in figure 7 corroborates the essence of the assumed nonlinear temperature perturbation.

3.4. *Buoyancy frequency as a function of buoyancy number*

The buoyancy of the lower layer, or the basal part of it, drives upward motion of the hot bottom layer against the chemical buoyancy of the overlying fluid, but ultimately diffusive loss of heat overwhelms that balance. Unlike the atmosphere or ocean, where inertia balances buoyancy, only diffusion can set the time scale for that balance.

The buoyancy of the heated, but intrinsically denser, bottom layer is the integral of density over the thickness of the layer:

$$\frac{\rho\alpha g \Delta T_1 d}{2} - \Delta\rho g d. \tag{23}$$

Material rises when the expression in (23) is positive. We may treat $\Delta T_1/2$ as the mean temperature anomaly in the layer. As a blob with mean temperature anomaly $\Delta T_1/2$ rises into the overlying fluid, diffusion of heat into the overlying fluid will cool it, and eventually the blob will lose its buoyancy.

Following Le Bars & Davaille (2004), we may approximate that time dependence by a factor $\exp(-t/\tau)$, where for the moment we leave τ unspecified. We may rewrite (23) as a condition on t; at $t = t_0$, $\rho\alpha\Delta T_1 \exp(-t_0/\tau) - 2\Delta\rho = 0$. Using the definition of B:

$$t_0 = -\tau \ln(2B). \tag{24}$$

Assuming that the diffusive time scale depends on the wavelength of the perturbation, λ, we have $\tau \sim \lambda^2/\kappa$. Non-dimensionalizing time using the Stokes speed and distance by the thickness of the layer and letting $\omega_C \sim 1/t_0$, (24) becomes:

$$\omega'_C \sim -\frac{k'^2}{Ra_1 \ln(2B)}. \tag{25}$$

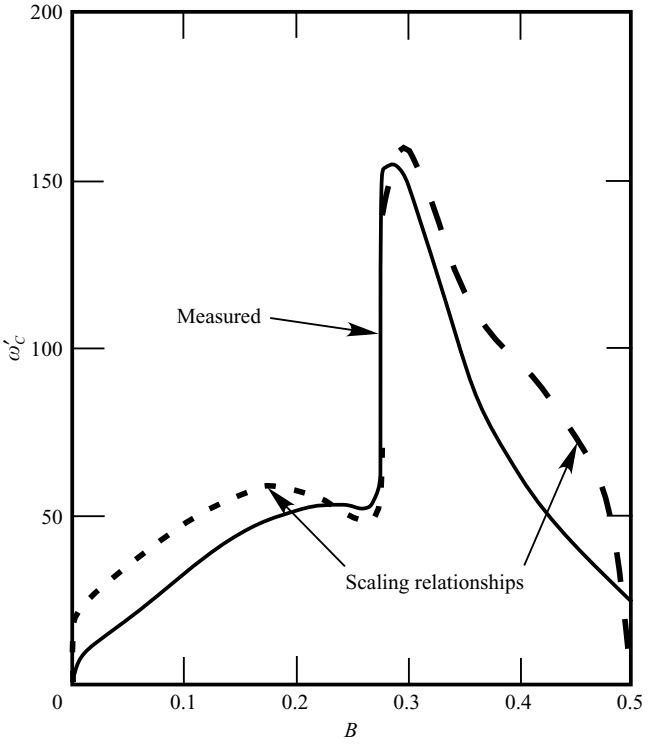

FIGURE 8. Comparison of scaling relationships derived on § 3.4 for ω'_C as a function of B. Those for both $B < \sim 0.275$ (short-dashed line) and $B > \sim 0.275$ (long dashed line) show similar forms, if not precise matches. $D/d = 19$; $\gamma = 100$.

We obtain a crude fit of (25) to calculated values of ω'_C *vs.* B for $0 \leqslant B \leqslant 1/4$ (figure 8) by choosing a coefficient of proportionality of 4.5 and using the calculated values of k'_C, i.e. $\omega'_C = -4.5k'^2_C/Ra_1 \ln(2B)$.

For $B > \sim 1/4$, instead of considering the buoyancy of the entire layer, we assume that the bottom, buoyant part of the chemically distinct layer must be buoyant enough to penetrate into the upper, negatively buoyant part of the layer. Material in the depth range $Bd < z \leqslant d$ is negatively buoyant, but material in the depth range $z < Bd$ is buoyant with respect to the material in the overlying layer. If the buoyancy of the lower part of the layer is impeded primarily by the negative buoyancy of its upper part, we have, by analogy with (23):

$$\int_0^{Bd} \left(\frac{\rho\alpha\Delta T_1}{d}[z-d] - \Delta\rho \right) \mathrm{d}z > \int_{Bd}^{d} \left(\frac{\rho\alpha\Delta T_1}{d}[z-d] - \Delta\rho \right) \mathrm{d}z. \tag{26}$$

This yields:

$$\rho\alpha\Delta T_1 \left[\frac{B^2-1}{2} \right] - \Delta\rho(1-B) > \rho\alpha\Delta T_1 \left[-\frac{B^2}{2} \right] - \Delta\rho B. \tag{27}$$

Again, allowing for an exponentially decaying time dependence of the temperature-dependent part and using the definition of B, (27) becomes:

$$(1-2B^2)\exp\left(-\frac{t_0}{\tau}\right) = 2B(1-2B). \tag{28}$$

Allowing $\omega \sim 1/t_0$, assuming $\tau \sim \lambda^2/\kappa$, and non-dimensionalizing yields:

$$\omega' \sim \frac{k'^2}{Ra_1 \ln\left[\dfrac{2B(1-2B)}{1-2B^2}\right]}. \tag{29}$$

A fit of (29) to calculated values of ω'_C *vs.* B for $B > \sim 1/4$ with the same coefficient of proportionality of 4.5 fits the observed dependence for a portion of this range of B (figure 8), if less well than (25) fits the lower range of B.

4. Laboratory experiments

4.1. *Laboratory set-up.*

To vary the viscosity and density contrasts between the two fluids, we added aqueous solutions of ammonium chloride salt and hydroxyethyl cellulose to water. The former allowed adjustment of the intrinsic density contrast and the latter was used to set the viscosities of the two fluid layers (Tait & Jaupart 1989). For all of the experiments discussed here, we used a rotating viscometer to measure the viscosity with an accuracy of about 10 %. For the small deformation rates of these experiments, such solutions behave as Newtonian fluids. Over the temperature range of this study, viscosity varied weakly with temperature, typically by 40 % for a temperature difference of 40 K, and most of our experiments explored a narrower range of temperature. We used the viscosity value for the average temperature, as is appropriate in variable viscosity fluids (White 1988). We measured the equation of state (density as a function of temperature) with a U-tube to an accuracy of 10^{-5}.

The walls of the experimental tank, 0.3 m × 0.3 m and 0.3 m high, are made of thick (30 mm) Plexiglas plates, which ensured thermal insulation for the duration of an experiment. The tank was set on a copper plate with internal circuitry connected to a bath whose temperature remained constant with spatial and temporal fluctuations smaller than 0.1 °C. The top of the upper liquid was a free surface in contact with air below a thick Plexiglas plate, which insulated the interior from the laboratory environment. We measured vertical temperature profiles using a thin thermocouple array. Temperatures were determined with an accuracy of 0.025 K and recorded every 30 s or 60 s, depending on the experiment.

All experiments followed the same protocol. The dense lower-layer liquid, coloured using food dye, was introduced at the base of the other intrinsically lighter fluid and left to spread horizontally until the interface was flat. The dye diffused across the interface into a very thin chemical boundary layer (typically one mm thick or less). Our greatest challenge was to generate a two-layer system with viscous miscible solutions and very small density differences (typically less than 1 %) without any mixing between the two liquids before they were heated. At time $t = 0$, the base plate was switched to a hot water bath and its temperature rapidly rose to a prescribed value.

The experimental values of the Rayleigh and buoyancy numbers are calculated with the total temperature difference ΔT because this was externally imposed. Because of the uncertainties in the physical properties of the fluids, we cannot test the theoretical predictions with great accuracy. Our goal was to establish the existence, in the relevant parameter ranges, of the two different types of instability (oscillatory and layered) and of the stable regime such that the lower layer was in thermal conductive equilibrium with heat flux extracted by small-scale convection at the interface. We carried out a

Exp. no	Ra†	B‡	η_1/η_2	Ra_2	Comments
GT01	551	0.15	5500	7.5×10^8	Oscillatory
GT03	135	0.14	5500	8.7×10^8	Oscillatory
GT25	564	0.46	5800	1.1×10^9	Oscillatory (barely)
LIZ01	1458	0.48	6600	3.5×10^8	Unstable (?)
LIZ03	142	0.10	6600	4.5×10^8	Oscillatory
LIZ15	376	0.38	1900	1.0×10^9	Oscillatory
LIZ16	227	0.94	2200	2.6×10^8	Stable
LIZ18	1508	0.72	690	5.2×10^8	Layered
LIT02	711	0.54	71	3.4×10^6	Stable
LIT05	1495	0.50	83	4.6×10^6	Layered
LIT06	1178	0.50	86	2.9×10^6	Oscillatory
LIT07	842	0.48	98	4.5×10^6	Stable
LIT08	526	0.63	65	2.9×10^6	Stable
LIT09	677	0.50	65	4.6×10^6	Oscillatory (barely)
LIT10	1209	0.67	65	2.8×10^5	Layered (barely)
LIT11	1027	0.56	69	6.4×10^6	Oscillatory (barely)
LIT12	1358	0.55	69	2.6×10^6	Layered
LIT13	1030	0.51	291	7.4×10^6	Oscillatory (barely)
LIT14	801	0.50	291	1.7×10^7	Stable
LIT15	1057	0.36	265	1.2×10^7	Oscillatory
LIT16	779	0.44	265	1.0×10^7	Oscillatory
LIT18	640	0.37	287	1.7×10^7	Oscillatory
LIT19	333	0.37	287	1.7×10^7	Oscillatory (barely)
LIT20	268	0.44	262	1.1×10^7	Stable
LIT22	1202	0.57	13	1.5×10^6	Unstable (?)
LIT23	1062	0.55	1500	4.5×10^7	Stable
LIT26	1230	0.30	1150	4.5×10^7	Oscillatory

†Values of the Rayleigh number are known with 10 % accuracy.
‡Experimental uncertainty on values of the buoyancy number is less than 1 %.

TABLE 1. Experiments.

large number of experiments to investigate the behaviour of the layered system over a wide range of parameters, but here, we focus on a restricted set of 27 experiments near the threshold of unstable flow (table 1). Also, two experiments far from this threshold will be used to illustrate the two basic flow patterns. We restricted the investigation to cases in which the lower liquid is the more viscous, largely because this configuration corresponds to the geological case motivating our study, but also because this makes creating the initial layered system without mixing much easier. Small Rayleigh numbers ($Ra < \sim 100$) are very difficult to achieve in the laboratory. They demand very thin layers and are relevant at very small buoyancy numbers, two conditions that require inordinately long times for the establishment of a flat interface between the two fluids. These limitations make the study of the stability curve for values of $B < 11/40$ difficult. For such small values of the buoyancy number, the critical Rayleigh number is also small, such that $\varepsilon_2 > 0.3$ in (4), implying that the convective boundary layer at the interface between the two fluids accounts for a large fraction of the total temperature contrast. In these cases, the idealized temperature structure used in our analysis (figure 1) may be too simplistic. This range of B values, however, is not relevant to the continental lithosphere, as we will show later.

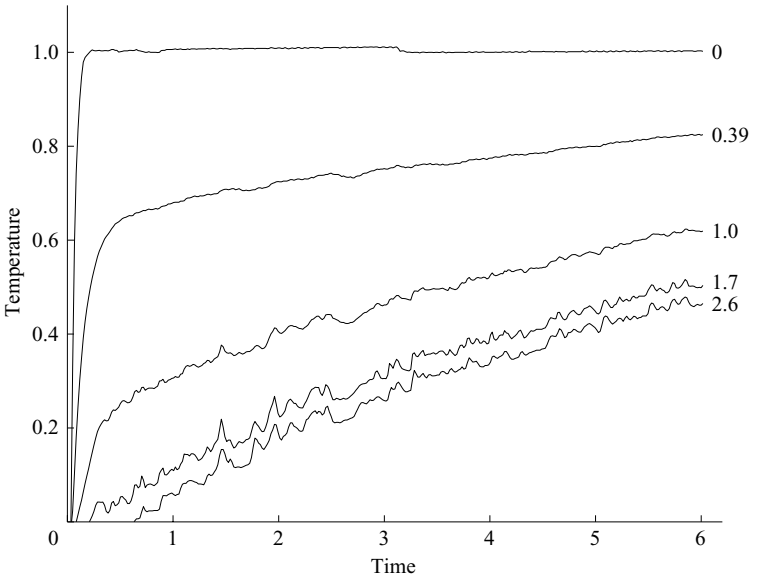

FIGURE 9. Dimensionless temperature ($T/\Delta T$) as a function of dimensionless time ($t' = t\kappa/d^2$) at various levels in the tank for experiment LIT20 (table 1). In this experiment at low Rayleigh number ($Ra = 268$), the lower layer was stable. $B = 0.44; \eta_1/\eta_2 = 260$. Note that the interface temperature (at $z' = 1.0$) begins to oscillate at a dimensionless time of about 0.25, which reflects the onset of small-scale convection in the thin thermal boundary layer that has developed in the upper layer made of low-viscosity fluid. The temperature grows slowly at all depths, as both fluids warm slowly. Note the almost linear temperature increase at all heights for times larger than about 1.4, which reflects the slow thermal evolution.

We present data from the experiments in dimensionless form. For discussion of the experiments, scaling time by the diffusive time scale for the lower layer (d^2/κ) allows proper evaluation of transients and of the time to reach thermal quasi-steady-state conditions in the lower layer. Perturbations to the thermal structure of the lower layer decay over time-spans shorter than this time scale; as shown below, a dimensionless time of about 1/4 elapses before a change of basal temperature propagates across the lower layer.

4.2. *A stable layer and quasi steady-state thermal structure*

For small values of Ra, a stable state should persist with the temperature difference across the lower layer, and the associated conductive heat flux, sustained by small-scale convection that develops at the interface between the two layers. Because we start heating the base of the lower layer at time $t = 0$, a finite time must elapse for a steady state to be reached. Heat diffuses through the dense lower layer and reaches the interface between the fluids, $z' = z/d = 1$, at $t' \approx 0.25$, when the rate of warming changes (figure 9). For the case in figure 9, LIT20 in table 1, carried out far below the stability curve ($Ra = 268$, $B = 0.44$), the temperature of the interface underwent small fluctuations superimposed on a gradual increase. We saw small wisps of coloured fluid (due to diffusion of the colouring agent into the upper layer) entrained by narrow plumes rising to the top of the tank. These plumes grew from instabilities of the thin thermal boundary layer that developed above the interface in the low-viscosity upper liquid. Such convective motion balances the heat flux into the lower layer, but because of the insulated top boundary, the whole upper layer must gradually warm (figure 9).

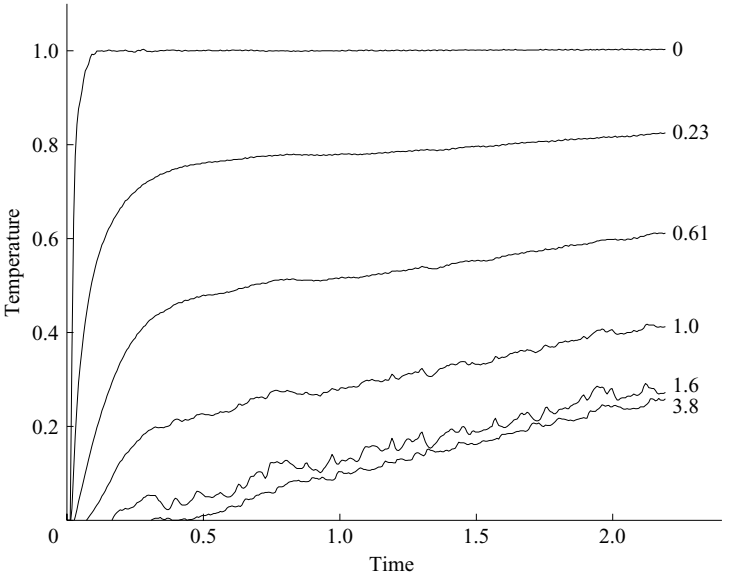

FIGURE 10. Dimensionless temperature as a function of dimensionless time for an experiment (LIT14, table 1) at Rayleigh number $Ra = 801$, close to the threshold of instability. $B = 0.50$; $\eta_1/\eta_2 = 291$. As for experiment LIT20 (figure 9), the lower layer remained stable, and small-scale convection at the interface allowed a quasi-steady-state thermal structure in the lower layer.

For $t' < \sim 0.25$, temperatures at the interface initially grow proportionally to $\sqrt{t'}$, as they should if controlled by diffusion. Later, temperatures adjust to an almost linear trend, as expected for the heating of the well-mixed upper layer at a nearly constant rate.

Because of the insulating top boundary, the temperature structure in our experiments cannot reach steady state. With the large volume of upper liquid, the time scale for its evolution is long compared to the diffusive time scale for the thin lower layer. For the experiment in figure 9, once small-scale convection has set in at the interface, the temperature difference between that in the upper layer and that at the base of the lower layer changes by only 10 % over a dimensionless elapsed time of 1. Remembering that it takes a dimensionless time of about 0.5 for a layer to reach equilibrium in diffusion with fixed temperature boundary conditions, we may therefore assume that the lower layer thermal structure is nearly steady state, such that the rate with which heat is extracted from the layer by small-scale convection is balanced by conductive heat transport through the layer. The Earth's lithosphere evolves similarly; the convecting mantle heats it from below as it cools at a low secular rate of about $100\,\mathrm{K\,Gyr^{-1}}$.

The same features as shown in figure 9 can be observed in an experiment carried out near the threshold of instability at an almost identical buoyancy number, $B = 0.50$ (LIT14, $Ra = 801$; figure 10). Again, for $t' > \sim 0.25$, small-scale convection generated temperature fluctuations at the interface. Such fluctuations, seen best just above the interface at $z' = 1.6$, propagated downward by diffusion into the lower liquid, but were damped with increasing distance from the interface. Their magnitudes are much smaller at $z' = 0.61$ and virtually absent at $z' = 0.23$. The temporal evolution of vertical temperature profiles for the same experiment (figure 11) shows that at $t' = 0.5$, an

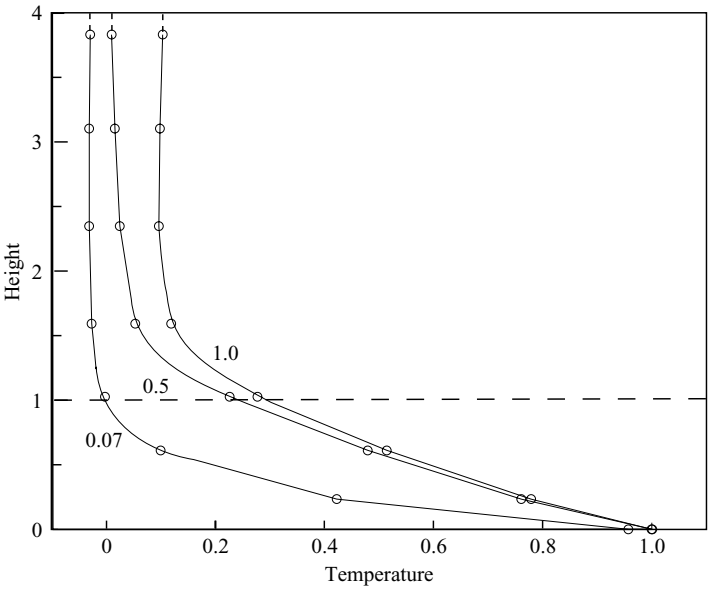

FIGURE 11. Dimensionless temperature as a function of dimensionless height above base in experiment LIT14 (table 1). $Ra = 801$; $B = 0.50$; $\eta_1/\eta_2 = 291$. The temperature gradient in the lower layer (between $z' = 0$ and $z' = 1$) is almost constant, and this gradient changes little between $t' = 0.5$ and $t' = 1.0$. Note the difference with the early profile at $t' = 0.07$, which has significant curvature.

almost linear temperature profile developed through the lower layer, corresponding to near equilibrium with the slowly varying heat flux due to small-scale convection at the interface. The difference between such a fully developed thermal structure and a transient one can be assessed by comparing the profiles for $t' = 0.07$, which shows marked curvature, with those for $t' = 0.5$ and $t' = 1.0$. Moreover, the two profiles at $t' = 0.5$ and $t' = 1.0$ differ little and closely match the idealized profile used in the marginal stability analysis (figure 1). We note that, in the fully developed regime at $t' = 0.5$, the temperature difference across the unstable boundary layer at the top of the lower layer is about 0.2, in agreement with the heat balance arguments developed above (equation (4)).

4.3. *Flow regimes*

For Rayleigh numbers sufficiently large, convection manifested itself either by alternating growth and decay of perturbations to the interface or by steady convection in the lower layer that deformed the interface. As shown by the analysis of marginal stability, which flow pattern occurred depends on the buoyancy number B and the critical Rayleigh number depends on its value.

At sufficiently low buoyancy number, domes and basins developed at the interface, and they rose and fell as an oscillating instability (figure 12). Upwelling flow in the lower fluid fed the domes as they grew, rising to variable heights depending on the Rayleigh number: the larger the Rayleigh number, the higher they rose. Eventually the intrinsically denser lower fluid in the domes equilibrated thermally with the surrounding fluid of the upper layer, and the domes fell back down. (At Rayleigh numbers several times the critical Rayleigh number, domes rose to the surface of the upper fluid and mixed with that layer by entraining the upper liquid as they fell back down. We will discuss this regime elsewhere.)

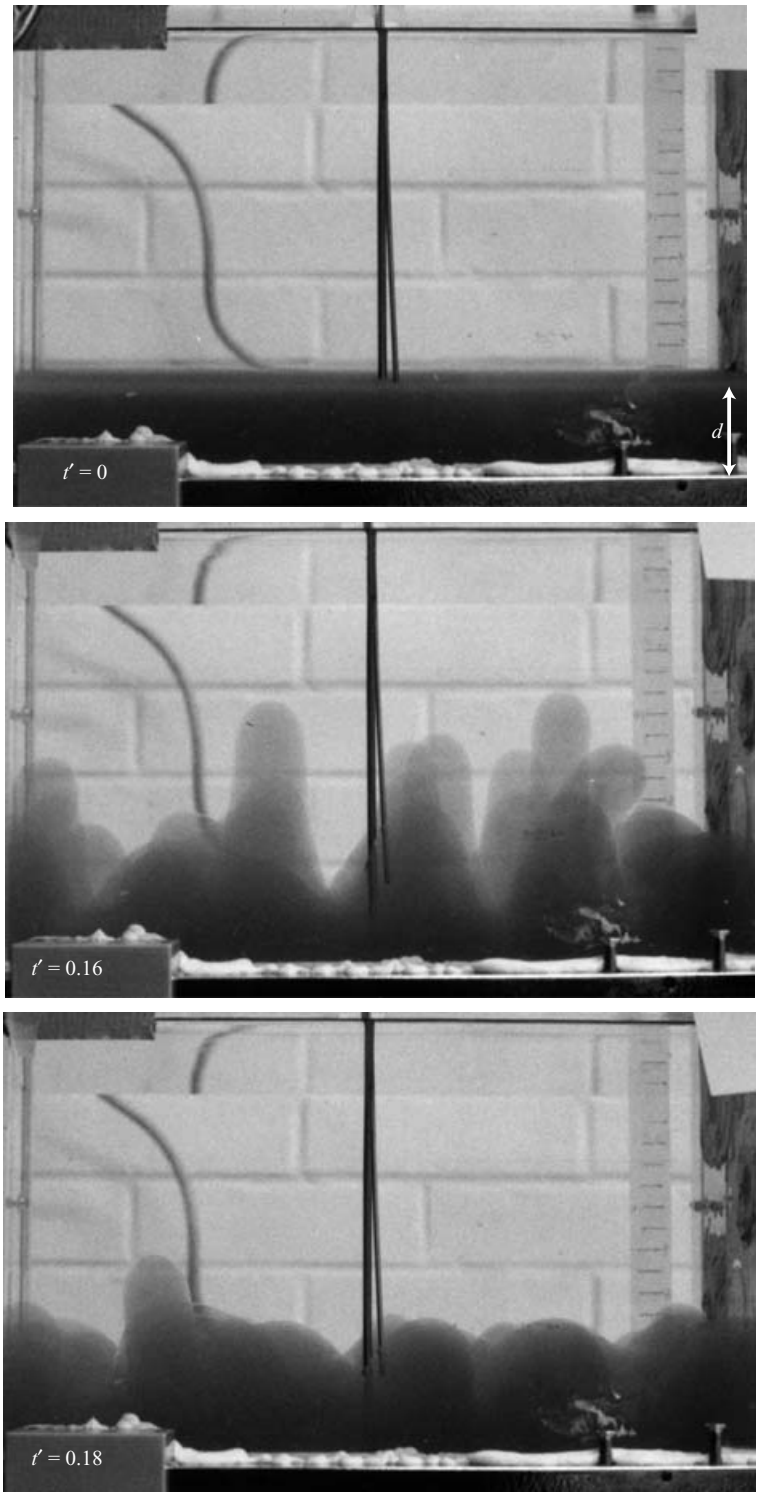

FIGURE 12. Photographs showing oscillatory convection during experiment LIZ12 ($Ra = 5.0 \times 10^3$, $B = 0.41$, $\gamma = 2.3 \times 10^3$) at three dimensionless times $t' = 0$, 0.16 and 0.18. In this experiment far from the stability threshold, the upwellings rise to large heights compared to the initial layer thickness d.

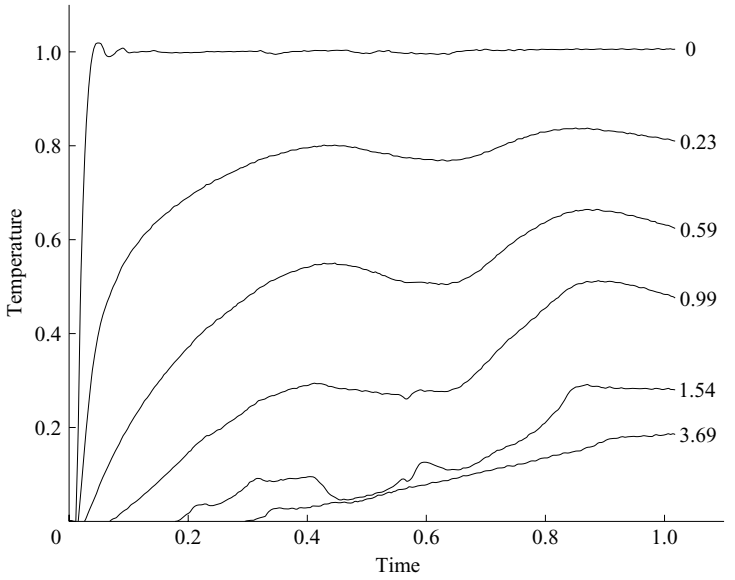

FIGURE 13. Dimensionless temperature as a function of dimensionless time for experiment LIT06 (table 1); large variations of temperature within the lower layer ($0 < z' \leqslant 1.0$) corroborate oscillatory convection that we observed visually. The Rayleigh number $Ra = 1178$ for this experiment at $B = 0.50$ is larger than the critical Rayleigh number ($Ra_C = 670$). $\eta_1/\eta_2 = 86$. The interface underwent large amplitude oscillations reaching heights $d_m/d = 2.2$.

This oscillatory flow leads to marked temperature oscillations throughout the tank, including the deep levels in the lower layer during the cycle of rising plumes and their collapse (figure 13). Compared with the data of figure 10, for which $Ra = 801$ and $B = 0.50$, those in figure 13, with a higher Rayleigh number $Ra = 1178$ and identical buoyancy number $B = 0.50$, show marked fluctuations in temperature. We observed this oscillatory convection regime at very small values of the Rayleigh number ($Ra = 135$, table 1) for the lower layer when the buoyancy number is small ($B < 0.3$), but for reasons given above, we could not run experiments at smaller Rayleigh numbers.

At large values of the buoyancy number, $B > \sim 0.5$, we observed a stable regime in which convection occurred in the lower layer, sustained by the heat flux across the interface. The interface developed a regular 'egg-box' shape with an easily measured characteristic wavelength (figure 14). For such cases, a steady convection regime developed, such that temperatures in the lower layer did not exhibit the marked oscillations of the oscillatory regime. The interface maintained its deformed shape. The 'layered' regime requires $Ra > 1000$, in contrast to the oscillatory regime and the planform of convection was hexagonal. Temperature recordings for an experiment in this regime are shown in figure 15 ($Ra = 1358$, $B = 0.55$, LIT12, table 1). In this experiment, the onset of small-scale convection was well-marked at $t' = 0.23$ as the upper layer began to heat up. The interface started to deform at $t' = 0.26$ and a fully-developed 'egg-box' interface was established at $t' \approx 0.36$ with domes that were twice as tall as the initial lower-layer thickness. In this case, the instability barely perturbed temperatures in the lower layer, in marked contrast to what happens in the oscillatory regime (figure 13).

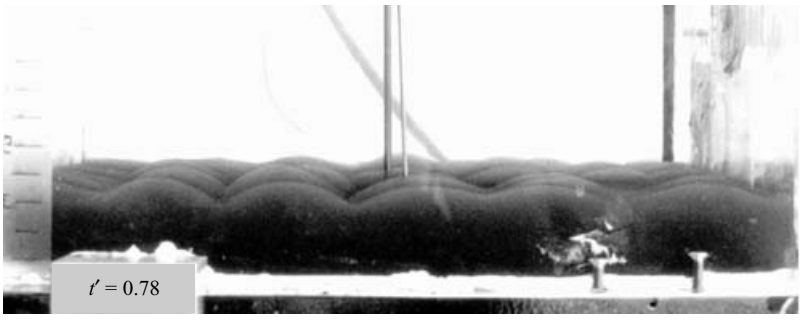

FIGURE 14. Photograph of experiment LIZ19 ($Ra = 1.6 \times 10^4$, $B = 0.72$ and $\gamma = 7.5 \times 10^2$), undergoing layered convection at $t' = 0.78$. The lower layer convects, and the interface deforms in response to that flow, but the large density of the lower layer prevents oscillatory flow.

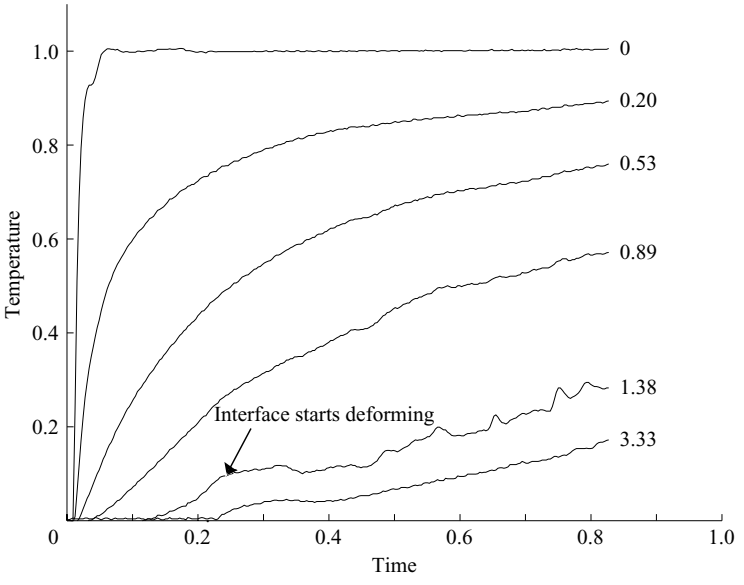

FIGURE 15. Dimensionless temperature as a function of dimensionless time for experiment LIT12 in the layered regime (table 1). These measurements can be best appreciated by comparing them to those for experiment LIT06 in figure 13, which correspond to similar values of the Rayleigh number and viscosity contrast and to a lower value of $B = 0.50$ (instead of 0.55 for experiment LIT12). $Ra = 1358$; $B = 0.55$; $\eta_1/\eta_2 = 69$. The onset of small-scale convection is pronounced at $t' = 0.23$ as temperatures near the top of the upper layer begin to rise. The interface between the two fluid layers started deforming at $t' = 0.25$. At $t' = 0.36$, the interface reached a stable configuration with large-amplitude deformation reaching heights $d_m/d = 2.1$, almost as large as in experiment LIT06 shown in figure 13. Yet, there was no marked change in the evolution of temperatures in the upper layer, in contrast to what occurred in experiment LIT06.

One potentially important factor is the influence of sidewalls on the flow field which is unaccounted for in the stability analysis. In the experiments for $B > 0.3$, the critical wavelength was a few times the bottom-layer thickness and there were between four and six fully developed upwellings over one tank-width. For $B < 0.3$, calculations predict very small values of the critical wavenumber and hence very large wavelengths, but we managed experiments only far above the stability curve. In those

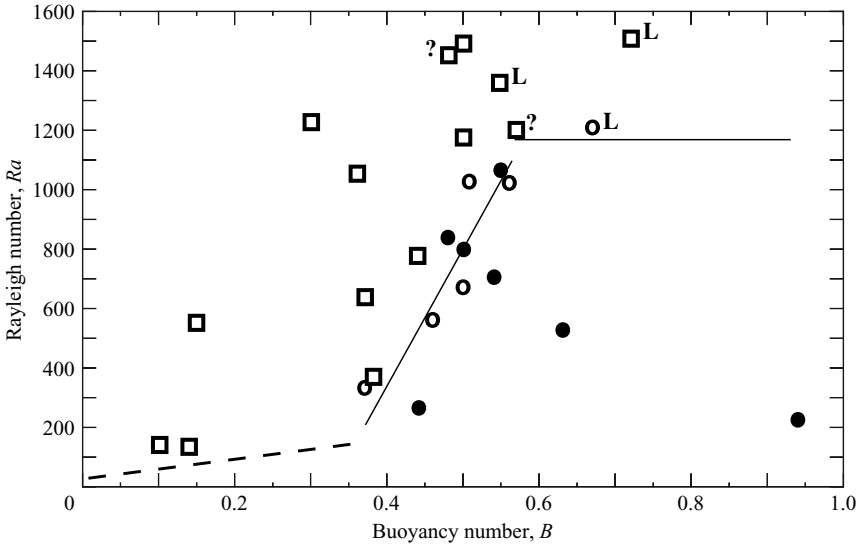

FIGURE 16. Regime diagram in *Ra vs*. *B* space. Open squares correspond to unstable situations manifested by oscillating domes and basins. Open circles correspond to experiments carried out close to marginal stability, which we assessed using the amplitude of the interface deformation (see table 2). Filled circles correspond to experiments with negligible flow in the lower layer. Symbols labelled 'L' correspond to experiments that were in the layered regime. Two experiments exhibited ambiguous flow patterns and are labelled '?' (see text for an explanation). Open symbols with no label correspond to experiments in the oscillatory regime.

cases, the Rayleigh number was larger than the critical value by a factor of about 3 and the wavelength was much smaller than the critical value. For example, we observed a pattern of four by four upwellings across the tank in experiment LIZ03 ($Ra = 142$, $B = 0.10$, table 1). In such conditions, we expect that the flow field was weakly affected by the presence of sidewalls.

4.4. *Stability diagram*

The 27 experiments (table 1) delineate roughly the stability curve in (Ra, B)-space (figure 16). We classified experiments in three groups. For the stable regime, we observed visually neither internal motion in the lower layer, nor deformation of interface and we recorded no temperature fluctuations in the lower layer. At the opposite extreme, fully developed instabilities were clear both visually and as recorded by temperature. A third group corresponds to experiments near stability, such that the magnitude either of sustained interface deformation or of heights above the base of the tank, d_m, of transient upwelling was small, $d_m/d < 1.5$. As shown in table 2, for a given value of B, this ratio decreases towards 1 with decreasing Ra, i.e. as Ra approaches the stability threshold. We used this behaviour to determine the critical Rayleigh number Ra_C for instability. For fixed B, we extrapolated the Ra versus d_m/d data to $d_m/d = 1$ (table 2), such that there is no deformation of the interface. This led to $Ra_C \approx 200$ for $B = 0.37$, $Ra_C \approx 500$ for $B = 0.45$ and $Ra_C \approx 670$ for $B = 0.50$. These results show that the critical Rayleigh number is an increasing function of the buoyancy ratio, in agreement with the trend predicted by the marginal stability analysis.

Experiments where instability occurred were also separated into two groups corresponding to the 'oscillatory' and 'layered' regimes (table 1). The former was such

Expt no.	Ra	B	η_1/η_2	d_m/d	λ/d	k'
LIT15	1057	0.36	265	5.0†	3.0	2.1
LIT18	640	0.37	287	2.4	3.6	1.7
LIT19	333	0.37	287	1.2	4.4	1.4
LIT16	779	0.44	265	2.1	3.1	2.0
GT25	564	0.46	5800	1.5	4.3	1.5
LIT06	1178	0.50	86	2.3	2.7	2.3
LIT13	1030	0.51	291	1.7	3.0	2.0
LIT09	677	0.50	65	1.0	3.3	1.9
LIT10	1209	0.67	65	1.1	2.3	2.7

†For this experiment, upwellings rose to the top of the upper layer.

TABLE 2. Wavenumber and interface deformation.

that we observed upwellings which rose and rapidly fell back down. The latter was such that the interface deformed and adopted a quasi-stable configuration which evolved slowly with time as the upper-layer temperature increased. Two experiments, LIZ01 and LIT22 (table 1), were ambiguous, with large and slow deformation of the interface, but rather small temperature fluctuations in the lower layer. These experiments are qualified as simply 'unstable' and labelled with a question mark in figure 16.

We could not define the threshold for the oscillatory mode at small buoyancy numbers, but experiments GT03 and LIZ03 at $B = 0.14$ and $B = 0.10$, respectively, and at $Ra \approx 140$, confirm the lack of stability at low Rayleigh numbers.

We did not examine the dependence on the viscosity contrast in detail, but we did carry out two experiments close to the stability curve with nearly identical values of Ra and B, with viscosity contrasts differing by almost one order of magnitude (LIZ15 and LIT19, table 1). We observed the same behaviour for each, consistent with the analysis of marginal stability. The viscosity contrast for all the experiments was larger than 10, and for such values theory indicates that results are not sensitive to the viscosity contrast (figure 4). Accordingly, we ignored the viscosity contrast in constructing figure 16. We also did not investigate the dependence of the critical Rayleigh number on the thickness ratio D/d because theory indicates that it is very small in the range of relevance to our experiments ($B > 0.3$; figure 4). Save for two exceptions, this ratio took values between 3.2 and 6.2 in the experiments given in table 1.

We did not attempt to determine accurately the critical Rayleigh number for the layered regime. In one experiment (LIT10, table 1) with $Ra \approx 1209$ and $B = 0.67$, very small, stable deformation of the interface ($d_m/d = 1.1$) indicates that it was carried out very close to stability. Moreover, the dimensionless wavenumber for this experiment of 2.7 (table 2), which we measured by counting the number of upwelling zones and scaling by the layer thickness, is very close to the theoretical value (figures 3 and 4). We take the Rayleigh number for this experiment as approximating the critical Rayleigh number for the layered regime.

The experimentally derived stability diagram (figure 16) was built in three steps. In the intermediate range of B values, we used the three critical values of the Rayleigh number determined above as well as two experiments at $B = 0.54$ and $B = 0.55$ which straddle the stability threshold. For small values of B, we could only determine upper bounds on the critical Rayleigh number. For values of B larger than 0.55, we relied on

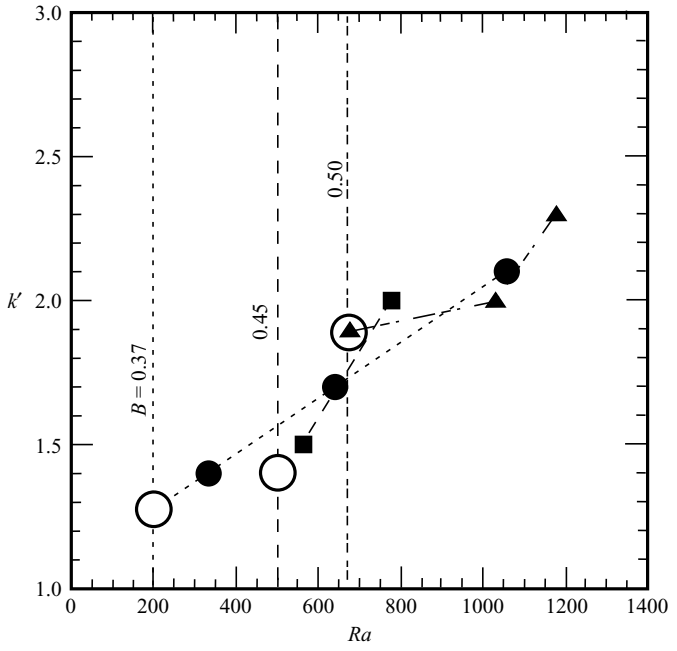

FIGURE 17. Plot of dimensionless wavenumbers k' as a function of Rayleigh number Ra for different values of buoyancy number B (table 2): ●, $B = 0.36$–0.37; ■, $B = 0.44$–0.46; ▲, $B = 0.50$–0.51. For each group, we extrapolate the relationship between k' and Ra to the approximate value of the critical Rayleigh number, Ra_C; ○, approximate values of k'_C for the corresponding values of B.

experiment LIT10, which, as explained above, was very close to stability, continuity with data at lower values of B as well as theoretical expectations. This stability diagram bears the same form as that derived for marginal stability (figures 3 and 4), but the observed stability curve is displaced to larger values of the buoyancy number than that for marginal stability. We attribute this difference to the presence of small-scale convection at the interface between the two liquids in the former, and its explicit omission in the latter. Such motion should enhance perturbations at the interface and therefore instability, and one may expect that a larger buoyancy ratio is required to ensure stability.

We estimated dimensionless wavenumbers corresponding to critical Rayleigh numbers by using experiments closest to the stability curve. For a given buoyancy number, the wavenumber increases as the Rayleigh number increases (figure 17, table 2). For each value of B, projecting the measured dependence of k' on Ra to its intercept with the estimated Ra_C yields an estimate of k'_C. As shown in figure 17, this yields values of $k'_C \approx 1.3$ for $B = 0.37$, $k'_C \approx 1.4$ for $B = 0.45$ and $k'_C = 1.9$ for $B = 0.50$. These values are in the range of values for marginal stability and reproduce the predicted trend of increasing critical wavenumber k'_C with increasing B (figures 3 and 4). Precise comparisons with theoretical values are unwarranted because of the simplifying assumptions that were made in the marginal stability analysis.

We determined the angular frequency of the oscillatory regime in a few cases. In a typical experiment, we waited for one full cycle of rise and fall and the start of a new cycle. The ratio between the diffusive time scale d^2/κ and the Stokes scaling used in the theory is the Rayleigh number for the lower layer, Ra. Thus, as B is

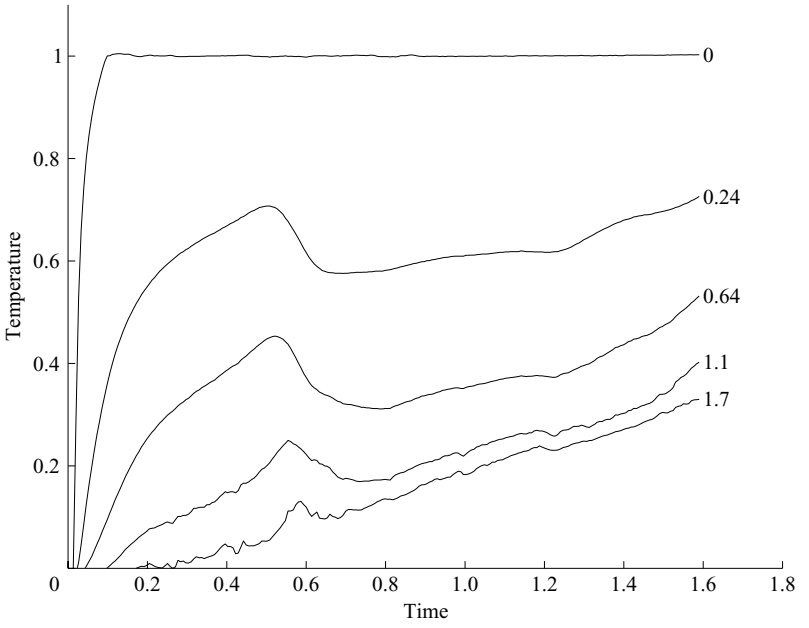

FIGURE 18. Dimensionless temperature as a function of dimensionless time for an experiment (LIT 26) in the oscillatory regime at a low value of the buoyancy number ($B = 0.30$) far from the stability curve. $Ra = 1230$; $\eta_1/\eta_2 = 1150$. For this experiment, $Ra \approx 4Ra_C$. These data should be compared to those for experiment LIT12 in the layered regime, which had an almost identical Rayleigh number ($Ra \approx 1300$) and a larger buoyancy number ($B = 0.55$), and which showed little variation in temperature (figure 15). By contrast, oscillatory convection manifests itself by large variations in temperature across the bottom layer in this low-buoyancy-number experiment. This comparison shows that the two different regimes persist to relatively large Rayleigh numbers.

decreased and hence as Ra_C decreases along the stability curve, oscillatory instability takes an increasingly longer time to develop. Figure 13 shows two complete cycles of rise and fall in an experiment with a Rayleigh number that was not much larger than the critical value (LIT06, $Ra = 1178$, $B = 0.50$, table 1). This allows a reliable determination of the dimensionless angular frequency $\omega' = 140 \times 10^{-4}$, which has the same order of magnitude as values along the theoretical stability curve (figure 3). The relationship between the frequency values at finite amplitude and in marginal stability conditions is likely to be complicated, as the former involve vertical flow over a finite distance.

4.5. *Finite-amplitude flow at supercritical Rayleigh numbers*

The experiments carried out for Rayleigh numbers many times Ra_C require an extensive report on their own. Here, we describe briefly some particular features.

The main boundary separating the two types of convective instability, defined by $B \approx 0.5$, applies at large values of the Rayleigh number. Two experiments carried out with nearly the same Ra (≈ 1300), but different values of B (0.30 and 0.55) show very different development (figures 15 and 18). For the larger value of B, temperature fluctuations are conspicuously absent in the lower layer, but for the smaller value of B, the large variations in temperature attest to oscillatory convection, as we observed.

The two regimes of convection differ not merely by their flow patterns and amplitudes of interface deformation, but also by the efficiency of mixing of the

two layers. For the Earth, the range of interest includes relatively small values of the Rayleigh number and we restrict the discussion to such conditions. In the layered regime at large values of the buoyancy number, convective downwelling in the lower layer entrains thin threads of the upper fluid into the lower layer. The low rate of mixing was too small to quantify accurately, though we did observe the mixing process in action. In the oscillatory regime, however, mixing proceeded in a different manner. The larger the Rayleigh number, the higher the upwelling plumes of lower fluid rose and the more contorted they became. After tall upwelling plumes reached their maximum heights, their downward fall did not proceed with the same smooth axisymmetric geometry. Instead, the tall fingers of lower fluid folded back onto themselves, encapsulated upper-layer fluid and dragged it downwards into the lower layer. Accordingly, the lower layer grew in thickness.

5. The continental lithosphere

Not only is continental lithosphere thick and chemically buoyant, but the thickness and intrinsic density are related to one another: the older the continent, the smaller its intrinsic density and the larger its thickness. Such a relationship is unlikely to arise by coincidence. Moreover, the buoyancy numbers of continents of various ages lie within the range for the oscillatory regime ($0.25 < B < 0.6$), for which such a relationship holds at marginal stability (Cottrell *et al.* 2004). An obvious question is, 'How did continental lithosphere reach this state?' This is not the place for a detailed discussion of the relevant geological processes and assessment of proposed explanations, but in the following, we comment briefly on the current interpretations and debates.

By analogy with the experiments described above (e.g. figures 12 and 13), the viscous buoyant layer in the Earth, the lithosphere, should undergo discrete instability events that are separated in time. During such events, downwelling plumes of cold, but intrinsically light material should sink into the underlying asthenosphere, and asthenospheric material should upwell where the lithosphere thins. Upwelling implies decompression of hot asthenosphere, which in turn implies melting and basaltic eruption. This melting has one crucial consequence: the mantle residue left by the extraction of melt should be intrinsically less dense than normal asthenosphere and hence should become part of a lithospheric root. In addition, where the lithosphere is stretched and thinned, the continental crust should also be subjected to divergent flow, thinning, and subsidence, so as to create space for sediment to accumulate. Above downwelling flow, the continental crust should undergo convergent flow, which leads to compressive features, such as folds and thrust faults.

The consolidation of Archean (age >2.5 Ga) lithosphere in South Africa seems to have occurred not in one event but in a series of discrete events within a relatively short time-span between 3.2 and 2.7 billions years (e.g. Shirey *et al.* 2002, 2003; Eglington and Armstrong 2004; Richardson, Shirey & Harris 2004). Near that time, two blocks, the Kaapvaal and Zimbabwe cratons and the intervening Limpopo Belt, a zone of compression, underwent major rifting events (indicating horizontal extension) and became buried by sediment. Simultaneously, basaltic eruption was widespread. Geochemical analysis of the basalt shows that it was extracted from the well-mixed convecting mantle. Peaks of geological activity were separated by about 200 million years (Eglington & Armstrong 2004). As discussed below, these events have been explained in other ways, with each event ascribed to a separate process. Yet, all of these geologic events are predictable consequences of the oscillatory convection that we discuss in the previous paragraph.

Although ancient continental interiors are commonly described as stable, many have been subjected to major perturbations, not just on their margins, but also within their interiors. For instance, at 2.1 Ga, the production of enormous quantities of basalt formed the Bushveld igneous complex in South Africa, the world's largest platinum repository. In North America, continental lithosphere was perturbed by the Keweenawan rift of 1.1 billion years ago and later by the formation of four intracratonic basins (Williston, Hudson Bay, Illinois and Michigan) about 500 million years ago. Such events occurred far from ocean basins and are not related to other tectonic events. For this reason, they have been explained as consequences of plumes of hot mantle impinging on the base of the lithosphere.

Part of the difficulty in interpreting the ancient rock record is the paucity of alternative phenomena whose powers of explanation can be compared against one another. Most geological interpretations rely on analogies with plate tectonics and hence on relative motion of oceanic plates. In this framework, events within continents are seen as processes responding to remotely applied forces to their boundaries. We recognize that many believe that these events mark collisions between cratons at subduction zones analogous to modern plate tectonic settings, but we are aware also that others have questioned such collisions and suggest that material assumed to have lain far away from cratons in fact is autochthonous to them (e.g. Prendergast 2004; Shimizu *et al.* 2004).

Suppose instead that the events at 3.2 and 3.0 Ga in South Africa reflect oscillatory convection in which blobs sank and then rose with an interval of 200 Myr between them. These events affected cratonic blocks with typical dimensions of ~500 km. From figure 3, we see that for $B > 0.3$, $\omega_c' \sim 50 - 150 \times 10^{-4}$. Rendering these dimensional gives for the period T of such oscillations:

$$T = \frac{2\pi}{\omega_c} = \frac{2\pi}{\omega_c'} \frac{\eta_l}{\rho \alpha \Delta T g d} \tag{30}$$

With $\eta_l = 10^{21}$ Pa s or 10^{22} Pa s, $\rho = 3.3 \times 10^3$ kg m^{-3}, $\alpha = 4 \times 10^{-5}$ °C^{-1}, $\Delta T \sim 1000$ °C, $g = 9.8$ m s^{-2} and $d = 150$ km, equation (30) gives $T \sim 130$ Myr to ~1.3 Gyr for $\omega_c' \sim 80 \times 10^{-4}$. Corresponding values of $k_C' \sim 1.5$–2 imply wavelengths of ~3–4 times the thickness of the layer, corresponding to lateral distances of ~400–600 km. Thus, a phenomenon proposed simply on fluid dynamical grounds and scaled to Earth-like conditions corresponds to periods and length scales appropriate to geological phenomena. Oscillatory convection might have been a crucial process in the consolidation of Archean and Proterozoic cratons.

We thank three anonymous referees for unusually thorough reviews and constructive comments. We also thank M. Le Bars and A. C. Molnar for assistance with the numerical analysis and A. Davaille and A. Namiki for helpful discussions. E. C. was funded by a Fulbright Fellowship and by the American Association of University Women. We all thank the Centre National de la Recherche Scientifique (CNRS), and P. M. acknowledges support from the National Science Foundation under grant NSF-EAR-0106909 and from the Miller Foundation of Berkeley where he worked on revisions. E. C. is now at the Smithsonian Institution Dept of Mineral Sciences.

Appendix A. Mathematical formalism

The governing equations can be written:

$$\nabla \cdot u_j = 0, \tag{A 1}$$

$$\rho\left[\frac{\partial}{\partial t}+u_j\cdot\nabla\right]u_j=-\nabla p_j+\rho\alpha g G_j z\hat{k}+\eta_j\nabla^2 u_i, \tag{A 2}$$

$$\left[\frac{\partial}{\partial t}+u_i\cdot\nabla\right]T=\kappa\nabla^2 T, \tag{A 3}$$

where subscript j takes values of 1 or 2 depending on the fluid layer. In the limit of small perturbations, equation (A3) becomes:

$$\frac{\partial}{\partial t}\vartheta_j-w_j G_j=\kappa\nabla^2\vartheta_j, \tag{A 4}$$

where ϑ_1 and ϑ_2 are perturbations to temperature in the two layers. To non-dimensionalize (A1), (A2) and (A4), we scale distances with the thickness of the lower layer, d, and velocity with the Stokes velocity for layer 1:

$$u_j=u_j' V=u_j'\left(\frac{\rho_0\alpha g G_1 d^3}{\eta_1}\right). \tag{A 5}$$

For time and pressure, we use

$$t=t'\frac{d}{V}=t'\left(\frac{\eta_1}{\rho_0\alpha g G_1 d^2}\right), \tag{A 6}$$

$$p=p'\frac{\eta_1 V}{d}=p'(\alpha\rho_0 g G_1 d^2). \tag{A 7}$$

As usual, primes indicate dimensionless quantities.

Equation (A2) now simplifies to:

$$\frac{Ra_1}{Pr}\frac{\partial u_j'}{\partial t'}=-\nabla' p_j'+\vartheta_j'\hat{k}+\frac{\eta_j}{\eta_1}\nabla'^2 u_j', \tag{A 8}$$

where the Rayleigh number is defined by (6) and the Prandtl number by $Pr=\nu_1/\kappa=\eta_1/\kappa\rho_0$. In the limit of infinite Prandtl number, the left-hand side of (A8) vanishes.

Following standard methods, we take the curl of (A8) to eliminate pressure, we then take the curl again, and finally we cross differentiate (A8) and (A4), to eliminate the perturbation to temperature. We obtain an equation solely in terms of the vertical component of velocity, w'.

$$\left(Ra\frac{\partial}{\partial t'}-\nabla'^2\right)\frac{\nu_j}{\nu_1}\nabla'^4 w_j'=-\frac{G_j}{G_1}Ra_1\frac{\partial^2 w_j'}{\partial x'^2}. \tag{A 9}$$

Dropping primes, we assume solutions of the form:

$$w_j\sim\exp(q_{ij}z+\mathrm{i}kx+st). \tag{A 10}$$

Substitution of (A10) into (A9) yields conditions on the values of q_{ij}

$$\frac{\nu_j}{\nu_1}\left(sRa+k^2-q_{ij}^2\right)\left(q_{ij}^2-k^2\right)^2=\frac{G_j}{G_1}k^2 Ra_1. \tag{A 11}$$

Thus, solutions to (A11) take the form

$$w_j(x,z,t)=\sum_{i=1}^{3}\left[A_{ij}\exp(q_{ij}z)+B_{ij}\exp(-q_{ij}z)\right]\exp(\mathrm{i}kx+st). \tag{A 12}$$

As usual, we then use boundary conditions to constrain A_{ij} and B_{ij}. At the bottom of the lower layer, $z=0$, we assume no vertical or horizontal components of velocity

and no perturbation to temperature:

$$w_1 = \partial w_1/\partial z = \nabla^4 w_1 = 0, \tag{A 13}$$

where the equation of continuity and incompressibility have been used. At the top of the upper layer, $z = D/d + 1$, we assume no vertical component of velocity, no shear stress, and no perturbation to temperature:

$$w_2 = \partial^2 w_2/\partial z^2 = \nabla^4 w_2 = 0, \tag{A 14}$$

where again the equation of continuity and incompressibility have been used. At the interface between the layers, $z = 1$, we assume continuity of both vertical and horizontal components of velocity:

$$w_1 - w_2 = 0, \tag{A 15}$$

$$\frac{\partial w_1}{\partial z} - \frac{\partial w_2}{\partial z} = 0. \tag{A 16}$$

We assume continuity of shear stress, τ_{xz}:

$$\frac{\partial^2 w_1}{\partial z^2} - \frac{\partial^2 w_1}{\partial x^2} - \frac{1}{\gamma}\left(\frac{\partial^2 w_2}{\partial z^2} - \frac{\partial^2 w_2}{\partial x^2}\right) = 0. \tag{A 17}$$

Continuity of normal stress yields (see Le Bars & Davaille 2002):

$$\nabla^2 \frac{\partial^2}{\partial t \partial z}(\gamma w_1 - w_2) + 2\frac{\partial^4}{\partial t \partial z \partial x^2}(\gamma w_1 - w_2) + \gamma B \frac{\partial^2 w_2}{\partial x^2} = 0. \tag{A 18}$$

Equation (A18) contains two important features: it provides the only place where the buoyancy number B appears, and it also introduces the angular frequency ω directly, through the differentiation by time, though ω also affects the values of q_{ij} in (A11). Continuity of perturbed temperature yields:

$$\gamma \nabla^4 w_1 - \nabla^4 w_2 = 0. \tag{A 19}$$

Continuity of the perturbed temperature gradient (heat flux) yields:

$$\gamma \nabla^4 \frac{\partial w_1}{\partial z} - \nabla^4 \frac{\partial w_2}{\partial z} = 0. \tag{A 20}$$

The boundary conditions in (A13)–(A20) place 12 conditions on the 6 values each of A_{ij} and B_{ij}. At the threshold of instability, the real part of s must vanish, but the imaginary part need not. Thus, we let $s = \mathrm{i}\omega$ in (A11), which defines values of q_{ij} as functions of k and ω. For all six values of A_{ij} and B_{ij} not to equal zero, the determinant of the matrix of their coefficients given by (A13)–(A20) must vanish. For selected values of B, G_2, γ and D, we sought values of Ra_1, k and ω for which the determinant vanished. We then sought the smallest value of the Rayleigh number, Ra_C, and the corresponding (dimensionless) values of wavenumber, k_C, and buoyancy frequency, ω_C.

Appendix B. The effect of the temperature gradient in the upper layer

We seek solutions for negligible temperature gradients in the upper layer. To determine what defines negligible, for selected values of B, γ and D, we calculated values of Ra_C for a wide range of values of G_2/G_1. For different values of γ and D, there exists a value of G_2/G_1 below which Ra_C becomes independent of G_2/G_1 (figure 19). Moreover, for sufficiently large values of G_2/G_1, Ra_C scales inversely with

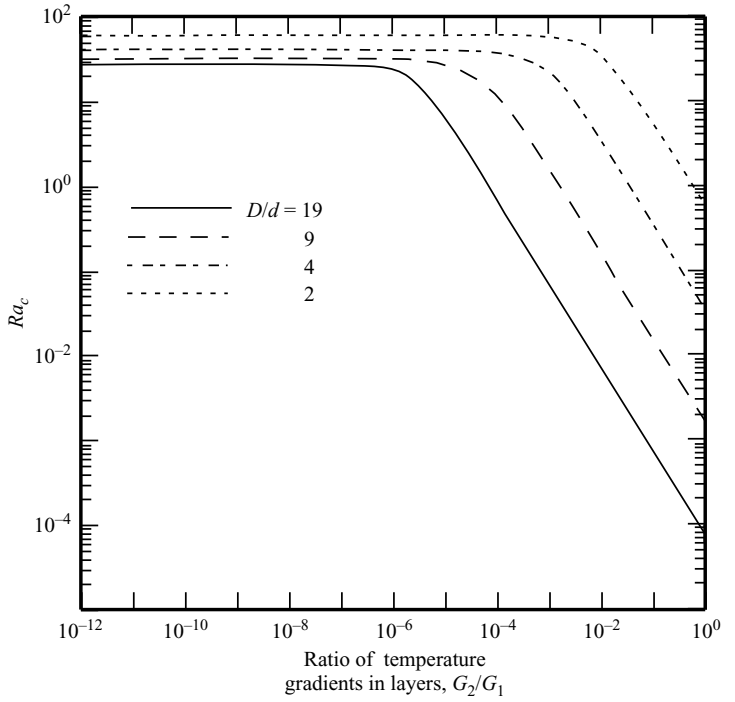

FIGURE 19. Dependence of Ra_C on G_2/G_1 for $B = 0.001$, $\gamma = 100$, and different values of D/d. Note that for sufficiently small temperature gradients in the upper layer, G_2, Ra_C is independent of G_2/G_1. For larger values of G_2/G_1, however, Ra_C decreases inversely proportionally to G_2/G_1, because in these cases, the upper layer becomes the unstable layer, not the lower one. In all calculations discussed in this paper, we used values of G_2/G_1 for which Ra_C is independent of G_2/G_1.

G_2/G_1. In this range, the upper layer is the more unstable layer, and convection develops faster within it. We define Ra_C in terms of properties of the lower layer, but if we used the upper layer, we would have an expression for the Rayleigh number Ra_{UL} given by

$$Ra_{UL} = \frac{G_2}{G_1}\gamma D^4 Ra_1. \tag{B 1}$$

Depending upon γ and D, there exists a value of G_2/G_1 for which Ra_{UL} should exceed its critical value. Then, as G_2/G_1 increases, Ra_{UL} equals that critical value, and as implied by (B1), Ra_C should decrease inversely with G_2/G_1 (figure 19). Moreover, when the upper layer is the more unstable, if the value of D increased two-fold, the value of Ra_C should decrease by 16 times, also shown in figure 19. All calculations discussed in the main text were made for values of G_2/G_1 such that Ra_C is independent of its value.

REFERENCES

CARLSON, R. W., BOYD, F. R., SHIREY, S. B., JANNEY, P. E., GROVE, T. L., BOWRING, S. A., SCHMITZ, M. D., DANN, J. C., PEARSON, D. G., BELL, D. R., GURNEY, J. J., RICHARDSON, S. H., TREDOUX, M., MENZIES, A. H., HART, R. J., WILSON, A. H. & MOSER, D. 2000 Continental growth, preservation and modification in southern Africa, *GSA Today* **10**, 1–6.

CHANDRASEKHAR, S. 1961 *Hydrodynamic and Hydromagnetic Stability*. Oxford University Press.

Cottrell, E., Jaupart, C. & Molnar, P. 2004 Marginal stability of thick continental lithosphere, *Geophys. Res. Lett.* **31**, L18612, doi:10.1029/2004GL020332.

Currie, I. G. 1967 The effect of heating rate on the stability of stationary fluids. *J. Fluid Mech.* **29**, 337–347.

Davaille, A. 1999*a* Two-layer thermal convection in miscible viscous fluids. *J. Fluid Mech.* **379**, 223–253.

Davaille, A. 1999*b* Simultaneous generation of hotspots and superswells by convection in a heterogeneous planetary mantle. *Nature* **402**, 756–760.

Davaille, A. & Jaupart, C. 1993 Transient high-Rayleigh-number thermal convection with large viscosity variations. *J. Fluid Mech.* **250**, 141–166.

Davaille, A. & Jaupart, C. 1994 Onset of thermal convection in fluids with temperature-dependent viscosity: application to the upper mantle. *J. Geophys. Res.* **99**, 19 853–19 866.

Davaille, A., Girard, F. & Le Bars, M. 2002 How to anchor hotspots in a convecting mantle? *Earth Planet. Sci. Lett.* **203**, 621–634.

Deardorff, J. W., Willis, G. E. & Lilly, D. K. 1969 Laboratory experiments of non-steady penetrative convection. *J. Fluid Mech.* **35**, 7–31.

Drazin, P. G. & Reid, W. H. 1981 *Hydrodynamic Stability*. Cambridge University Press.

Doin, M.-P., Fleitout, L. & McKenzie, D. 1996 Geoid anomalies and the structure of continental and oceanic lithospheres. *J. Geophys. Res.* **101**, 16 119–16 135.

Eglington, B. M. & Armstrong, R. A. 2004 The Kaapvaal Craton and adjacent orogens, southern Africa: a geochronological database and overview of the geological development of the craton. *South African J. Geol.* **107**, 13–32.

Gonnermann, H. M., Manga, M. & Jellinek, A. M. 2002 Dynamics and longevity of an initially stratified mantle. *Geophys. Res. Lett.* **29**(10), 1399, doi:10.1029/2002GL01485.

Gung, Y., Panning, M. & Romanowicz, B. 2003 Global anisotropy and the thickness of continents. *Nature*, **422**, 707–711.

Hirth, G. & Kohlstedt, D. L. 1996 Water in the oceanic upper mantle: implications for rheology, melt extraction and the evolution of the lithosphere. *Earth Planet. Sci. Lett.* **144**, 93–108.

Houseman, G. A. & Houseman, D. K. 2006 Stability and periodicity in the thermal and mechanical evolution of continental tectonics. *Geophys. J. Intl* (submitted).

Howard, L. N. 1966 Convection at high Rayleigh numbers. In *Proc. 11th Intl Congress of Applied Maths*, (ed. H. Görtler). pp. 1109–1115. Springer.

Hsui, A. T. & Riahi, D. N. 2001 Onset of thermal chemical convection with crystallization and its geological implications. *Geochem. Geophys. Geosyst.* **2**(4), doi: 10.1029/2000GC000075.

Jaupart, C. & Mareschal, J. C. 1999 The thermal structure and thickness of continental roots. *Lithos* **48**, 93–114.

Jaupart, C. & Tait, S. 1995 The dynamics of differentiation in magma chambers. *J. Geophys. Res.* **100**, 17 615–17 636.

Jaupart, C., Mareschal, J. C., Guillou-Frottier, L. & Davaille, A. 1998 Heat flow and thickness of the lithosphere in the Canadian Shield. *J. Geophys. Res.* **103**, 15 269–15 286.

Jellinek, A. M. & Manga, M. 2002 The influence of a chemical boundary layer on the fixity, spacing and lifetime of mantle plumes. *Nature* **418**, 760–763.

Jellinek, A. M. & Manga, M. 2004 Links between long-lived hot spots, mantle plumes, D", and plate tectonics. *Rev. Geophys.* **42**, RG3002, doi:10.1029/2003RG000144.

Jordan, T. H. 1975 The continental tectosphere. *Rev. Geophys. Space Phys.* **13**, 1–12.

Jordan, T. H. 1978 Composition and development of the continental tectosphere. *Nature* **274**, 544–548.

Jordan, T. H. 1988 Structure and formation of the continental tectosphere. *J. Petrol. Special Lithosphere Issue*, pp. 11–37.

Kohlstedt, D. L., Evans, B. & Mackwell, S. J. 1995 Strength of the lithosphere: constraints imposed by laboratory experiments. *J. Geophys. Res.* **100**, 17 587–17 602.

Lay T., Garnero, E. J., Young, C. J. & Gaherty, J. B. 1997 Scale length of shear velocity heterogeneity at the base of the mantle from S wave differential travel times. *J. Geophys. Res.* **102**, 9887–9909.

Le Bars, M. & Davaille, A. 2002 Stability of thermal convection in two superimposed miscible viscous fluids. *J. Fluid Mech.* **471**, 339–363.

Le Bars, M. & Davaille, A. 2004 Large interface deformation in two-layer thermal convection of miscible viscous fluids. *J. Fluid Mech.* **499**, 75–110.

Lister, C. R. B., Sclater, J. G., Davis, E. E., Villinger, H. & Nagihara, S. 1990 Heat flow maintained in ocean basins of great age: investigations in the north-equatorial Pacific. *Geophys. J. Intl* **102**, 603–630.

McNamara, A. K. & Zhong, S. 2004*a* Thermochemical structures within a spherical mantle: Superplumes or piles? *J. Geophys. Res.* **109**, B07402, doi:10.1029/2003JB002847.

McNamara, A. K & Zhong, S. 2004*b* The influence of thermochemical convection on the fixity of mantle plumes. *Earth Planet. Sci. Lett.* **222**, 485–500.

McNamara, A. K. & Zhong, S. 2005 Thermochemical structures beneath Africa and the Pacific Ocean. *Nature* **437**, 1136–1139.

Namiki, A. 2003 Can the mantle entrain D"? *J. Geophys. Res.* **108**(B10), 2487, doi:10.1029/2002JB002315.

Namiki, A. & Kurita, K. 2003 Heat transfer and interfacial temperature of two-layered convection: Implications for the D"-mantle coupling. *Geophys. Res. Lett.* **30**(1), 1023, doi:10.1029/2002GL015809.

Olson, P. & Kincaid, C. 1991 Experiments on the interaction of thermal convection and compositional layering at the base of the mantle. *J. Geophys. Res.* **96**, 4347–4354.

Parsons, B. & McKenzie, D. 1978 Mantle convection and the thermal structure of the plates. *J. Geophys. Res.* **83**, 4485–4496.

Parsons, B. & Sclater, J. G. 1977 An analysis of the variation of ocean floor bathymetry and heat flow with age. *J. Geophys. Res.* **82**, 803–827.

Pearson, D. G., Carlson, R. W., Shirey, S. B., Boyd, F. R. & Nixon, P. H. 1995 The stabilisation of Archaean lithospheric mantle: a Re–Os isotope study of peridotite xenoliths from the Kaapvaal craton. *Earth Planet. Sci. Lett.* **134**, 341–357.

Pellew, A. & Southwell, R. V. 1940 On maintained convective motion in a fluid heated from below. *Proc. Roy. Soc.* A **176**, 312–343.

Poudjom Djomani, Y. H., O'Reilly, S. Y., Griffin, W. L. & Morgan, P. 2001 The density structure of subcontinental lithosphere through time. *Earth Planet. Sci. Lett.* **184**, 605–621.

Prendergast, M. D. 2004 The Bulawayan Supergroup: a late Archaean passive margin-related large igneous province in the Zimbabwe craton. *J. geol. Soc., Lond.* **161**, 431–445.

Richardson, S. H., Gurney, J. J., Erlank, E. J. & Harris, J. W. 1984 Origin of diamonds in old enriched mantle. *Nature* **310**, 198–202.

Richardson, S. H., Shirey, S. B. & Harris, J. W. 2004 Episodic diamond genesis at Jwaneng, Botswana, and implications for Kaapvaal craton evolution. *Lithos* **77**, 143–154.

Richter, F. M. & Johnson, C. E. 1974 Stability of a chemically layered mantle. *J. Geophys. Res.* **79**, 1635–1639.

Rudnick, R. L., McDonough, W. F. & O'Connell, R. J. 1998 Thermal structure, thickness and composition of continental lithosphere. *Chem. Geol.* **145**, 399–416.

Shimizu, K., Nakamura, E., Kobayashi, K. & Maruyama, S. 2004 Discovery of Archean continental and mantle fragments inferred from xenocrysts in komatiites, the Belingwe greenstone belt, Zimbabwe. *Geology* **32**, 285–288.

Shirey, S. B., Harris, J. W., Richardson, S. H., Fouch, M. J., James, D. E., Cartigny, P., Deines, P. & Viljoen, F. 2002 Diamond genesis, seismic structure & evolution of the Kaapvaal-Zimbabwe craton. *Science* **297**, 1683–1686.

Shirey, S. B., Harris, J. W., Richardson, S. H., Fouch, M. J., James, D. E., Cartigny, P., Deines, P. & Viljoen, F. 2003 Regional patterns in the paragenesis and age of inclusions in diamond, diamond composition & the lithospheric seismic structure of Southern Africa. *Lithos* **71**, 243–258.

Tackley, P. J. 1998 Three-dimensional simulations of mantle convection with a thermochemical CMB boundary layer: D"? In *The Core–Mantle Boundary Region* (ed. M. Gurnis, M. E. Wysession, E. Knittle & B. A. Buffett), pp. 231–253, American Geophysical Union.

Tait, S. & Jaupart, C. 1989 Compositional convection in viscous melts. *Nature* **338**, 571–574.

Townsend, A. A. 1964 Natural convection in water over an ice surface. *Q. J. R. Met. Soc.* **90**, 248–259.

Wenzel, M. J., Manga, M. & Jellinek, A. M. 2004 Tharsis as a consequence of Mars' dichotomy and layered mantle. *Geophys. Res. Lett.* **31**, L04702, doi:10.1029/2003GL019306.

White, D. B. 1988 The planforms and onset of convection with a temperature-dependent viscosity. *J. Fluid Mech* **191**, 247–286.

Worster, M. G. 2004 Time-dependent fluxes across double-diffusive interfaces. *J. Fluid Mech.* **505**, 287–307.

Zaranek, S. E. & Parmentier, E. M. 2004 Convective cooling of an initially stably stratified fluid with temperature-dependent viscosity: implications for the role of solid-state convection in planetary evolution. *J. Geophys. Res.* **109**, B03409, doi:10.1029/2003JB002462.

Zhong, S. & Hager, B. H. 2003 Entrainment of a dense layer by thermal plumes. *Geophys. J. Int.* **154**, 666–676.